

Fractional Quantum Zeno Effect Emerging from Non-Hermitian Physics

Yue Sun,^{1,2} Tao Shi,^{3,4,*} Zhiyong Liu,^{5,6} Zhidong Zhang,^{5,6} Liantuan Xiao,^{1,2} Suotang Jia,^{1,2} Ying Hu^{1,2,†}

¹State Key Laboratory of Quantum Optics and Quantum Optics Devices,
Institute of Laser Spectroscopy, Shanxi University, Taiyuan 030006, China

²Collaborative Innovation Center of Extreme Optics, Shanxi University, Taiyuan 030006, China

³CAS Key Laboratory of Theoretical Physics, Institute of Theoretical Physics,
Chinese Academy of Sciences, Beijing 100190, China

⁴CAS Center for Excellence in Topological Quantum Computation,
University of Chinese Academy of Sciences, Beijing 100049, China

⁵Shenyang National Laboratory for Materials Science, Institute of Metal Research,
Chinese Academy of Sciences, Shenyang 110016, China

⁶School of Materials Science and Engineering, University of Science and Technology of China, Shenyang 110016, China

Exploring non-Hermitian phenomenology is an exciting frontier of modern physics. However, the demonstration of a non-Hermitian phenomenon that is quantum in nature has remained elusive. Here, we predict quantum non-Hermitian phenomena: the fractional quantum Zeno (FQZ) effect and FQZ-induced photon antibunching. We consider a quantum optics platform with reservoir engineering, where nonlinear emitters are coupled to a bath of decaying bosonic modes whose own decay rates form band structures. By engineering the dissipation band, the spontaneous emission of emitters can be suppressed by strong dissipation through an algebraic scaling with fractional exponents—the FQZ effect. This fractional scaling originates uniquely from the divergent dissipative density of states near the dissipation band edge, different from the traditional closed-bath context. We find FQZ-induced strong photon antibunching in the steady state of a driven emitter even for weak nonlinearities. Remarkably, we identify that the sub-Poissonian quantum statistics of photons, which has no classical analogs, stems here from the key role of non-Hermiticity. Our setup is experimentally feasible with the techniques used to design lattice models with dissipative couplings.

I. INTRODUCTION

While enchanting non-Hermitian properties unattainable in Hermitian systems are widely revealed [1–10], genuine quantum non-Hermitian phenomenology is still largely uncharted territory. For a classical system, coupling to an environment induces dissipation and can be well described by a non-Hermitian Hamiltonian. On the quantum level, however, dissipation occurs with quantum fluctuations, something fundamentally absent in the classical regime. Exploring quantum non-Hermitian phenomena, thus, involves identifying observable consequences driven by the role of non-Hermiticity amid quantum fluctuations. In this direction, the possibility to ingeniously design dissipation with quantum materials enables unique opportunities. Experimentally, non-Hermitian physics such as parity-time symmetry [1] were simulated with photons [11–13], atoms [14–18], electronic spins [19], and superconducting qubits [20]. Recently, realizations of dissipative couplings with an array of photonic resonators [21], atomic spin waves [17], or polaritons [22, 23] coupled to a reservoir have led to engineered dissipative lattice models with non-Hermitian bands. However, the observed phenomena to date were classical in nature. Theoretically, non-Hermitian effects under the quantum mechanical framework are being actively pursued [24–30], but the difficulty to tackle the dynamical long-time behaviors of open many-body quantum systems has severely limited these studies to single-particle physics and short timescales. Though highly

sought after, unambiguous quantum non-Hermitian phenomenon have remained elusive so far.

Here, we predict quantum non-Hermitian phenomena—the fractional quantum Zeno (FQZ) effect and FQZ-induced photon antibunching, based on a quantum optics setup harnessing reservoir engineering [31–41]. The system consists of nonlinear quantum emitters, such as atoms and artificial atoms, which host multiple excitations with nonlinear interactions. We exploit an engineered “open bath” represented by a continuum of decaying bosonic modes in a lattice with dissipative couplings, whose own dissipation rates form band structures. Different from previous reservoir engineering, which designs the energy dispersion of a closed medium, we manipulate the dissipation band of the open bath to dynamically tailor the system-bath interaction. As the central result, we show the FQZ effect emerging in the long-time emitter dynamics, where the spontaneous emission of emitters is dissipatively suppressed according to an algebraic scaling with fractional exponents. The scaling behaviors of $n = 1, 2, \dots$ excitations, moreover, are distinct, which can be controlled via the detuning of emitters. By analyzing the steady-state second-order correlation function of the weakly driven emitter, we show strong, FQZ-induced photon antibunching even for a weak nonlinearity. Different from conventional quantum light generation [42–44], the present sub-Poissonian quantum statistics of photons is driven by structured dissipation captured by a non-Hermitian Hamiltonian, which opens the door to exploring non-Hermitian quantum optics.

The FQZ effect predicted here is conceptually different

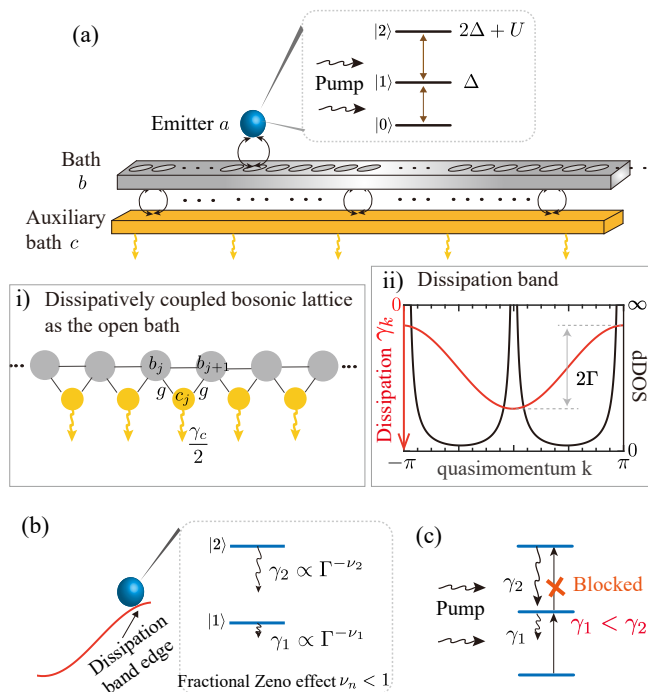


Figure 1. Illustration of a nonlinear emitter coupled to a 1D open bath and the fractional quantum Zeno (FQZ) effect. (a) Setup. An emitter a (blue ball) is coupled to a bosonic bath b (gray). The bath b is coupled to the auxiliary bath c (yellow). Top: energy levels of a driven emitter with n excitations ($n = 0, 1, 2$), where Δ is the detuning from the central frequency of the bath b and U is the strength of nonlinear interaction. (i) Engineered open bath for the emitter. Bosonic mode b_j in a lattice of N_b sites, in general, has the tunneling rate J and phase θ . The auxiliary modes c_j have the common, large loss rate $\gamma_c/2$. Both b_j and b_{j+1} are coupled to the lossy mode c_j with the coupling rate g ($j = 1, \dots, N_b - 1$). This engineers a dissipative coupling between b_j and b_{j+1} with the rate $\Gamma/2$, where $\Gamma = 4g^2/\gamma_c$ [cf. Eq. (5)]. (ii) The open bath exhibits the dissipation band γ_k (red curve) with the bandwidth 2Γ . The corresponding dissipative density of states (dDOS) is shown by the black curve. (b) FQZ effect. Strong dissipation $\Gamma \gg 2J$ confines the emitter to the dissipation band edge with divergent dDOS. This leads to the FQZ effect and a multi-excitation quasibound state: Their decay rate $\gamma_n \propto \Gamma^{-\nu_n}$ ($\nu_n < 1$ for $n = 1, 2$) is suppressed by large Γ via the scaling with fractional exponent ν_n . (c) FQZ-induced photon antibunching. The n -dependent FQZ effects allow one to engineer $\gamma_1 < \gamma_2$ in such a way to enable photon blockade in the emitter even for weak nonlinearity U .

from the familiar nonanalytic phenomena in quantum optics and condensed matter physics. It generically results from the combination of strong dissipation and a divergent *dissipative* density of states (dDOS) — the number of bath modes with a particular dissipation rate — near the dissipation band edge. In the closed-bath context, including the extensively studied spin-boson problems in quantum optics and various impurity models in condensed matter physics [45–48], the system-bath inter-

action is constrained by energy conservation. Instead, our setup has the distinctive feature that such energetic constraint is removed owing to the open nature of the bath. Thus, while gapless modes are crucial for conventional nonanalytic phenomena [47], the present fractional scaling is possible regardless of whether or not the bath has gapless energy or dissipation spectra. It further has the unique property where the scalings of n -excitation states are different for various n , which cannot occur in platforms with the closed bath [39, 48–62], including nanophotonic systems and solid-state band-gap materials, where the resonance condition locks the emitter with the bath energetically. As an important consequence, we show the sub-Poissonian quantum statistics of photons resulting from the key role of non-Hermiticity.

We also emphasize a novel approach based on the Keldysh formalism for efficient solutions of the *full* dynamics of nonlinear emitters immersed in the open bath. In particular, we are able to identify the role played by non-Hermitian Hamiltonians in the steady-state quantum correlation functions of the weakly driven emitters, capitalizing on a deep relation [63, 64] between the master equation and the scattering theory. Mathematically, compared with the established Green function approach associated with the closed bath, the open bath enriches the analytic structure of the emitter Green functions: The branch cut corresponding to the continuum generally becomes a “branch circle” instead of a line, which challenges the studies of quantum few-body and many-body dynamics. We circumvent this difficulty by introducing the effective fictitious bath.

The phenomena and principles described here exist for a wide class of dissipation band structures and for the open bath in arbitrary dimensions. Our results are also of relevance for current experiments with quantum materials, where realizing dissipative lattice models and engineering non-Hermitian band structures are state of the art, while demonstrating quantum non-Hermitian phenomena has remained an open challenge.

We begin in Sec. II by outlining the main results and their implications. In Sec. III, we describe the quantum mechanical model of emitters coupled to a one-dimensional (1D) open bath. In Sec. IV, we develop the general formalism for solutions of the dynamics and quantum correlations of weakly driven emitters. In Sec. V, we study the spontaneous emission of an emitter with single and two excitations, respectively, and show the FQZ effect. We also study the quantum correlation between two emitters. In Sec. VI, we analyze the second-order correlation function of a weakly driven emitter and show FQZ-induced sub-Poissonian light generation. In Sec. VII, we present a scaling analysis for the arbitrary bath. In Sec. VIII, we discuss the experimental implementations, and we conclude our paper in Sec. IX.

II. OVERVIEW OF MAIN RESULTS

Our setup is illustrated in Fig. 1(a), where one or several emitters are coupled to an engineered bosonic open bath in one dimension. The emitter is nonlinear with multiple bosonic excitations and is weakly driven by an external field. This may be cavities with Kerr interactions or two-level systems in the limit of infinite repulsive interactions. The emitters and the open bath *as a whole* constitute an open quantum system whose dynamics is governed by a master equation (see Sec. III): It contains a time evolution governed by an effective non-Hermitian emitter-bath Hamiltonian and quantum jumps [65, 66] associated with the emission of quanta from the open bath into the auxiliary reservoir [Fig. 1(a)]. The effective Hamiltonian associated with the open bath describes a dissipative lattice with an energy band $\epsilon_k = 2J \sin(k + \theta)$ and a dissipation band $\gamma_k = \Gamma(1 + \cos k)$. In the limit of $\Gamma/(2J) \rightarrow 0$, the closed bath is recovered, where the rich physics of various impurity models has been extensively studied ranging from quantum optics [46–48] to condensed matter physics [45].

Instead, we are interested in the unexplored physics in the strong dissipation limit $\Gamma/(2J) \gg 1$, where the interaction between the emitters and the open bath is no longer restricted by energy conservation, and the dissipation band γ_k is expected to play the central role in determining quantum emissions. Analogous to the density of states associated with energy dispersion, we characterize the dissipation band with the dDOS, i.e., the number of modes $D_s(\gamma)$ at the dissipation rate γ . In 1D, we have

$$D_s(\gamma) \propto \left| \frac{1}{\partial_k \gamma_k} \right|. \quad (1)$$

We explore how $\gamma(k)$ and dDOS influence the spontaneous emissions of multiple excitations of emitters and their statistics as quantified by the second-order correlation function.

It is challenging to solve the master equation of the entire open system consisting of the emitters and the open bath, when the emitters are highly nonlinear and externally driven. In particular, it is difficult to pinpoint the role played by the non-Hermitian Hamiltonian in the dynamical long-time behaviors of the emitters. We address this challenge by developing a framework based on the Keldysh formalism [67, 68] and the scattering theory.

Our road map consists of two steps (see Sec. IV). First, we develop an efficient approach to solve the spontaneous emission of multiple excitations in nonlinear emitters without driving, based on the Keldysh formalism (Fig. 2). With respect to the Green function approach associated with the closed bath, the open bath significantly enriches the analytic structure of the emitter Green function. Here, the branch cut corresponding to the continuum generally becomes a “branch circle” instead of a line, which separates the first Riemann surface to two disconnected regions, and challenges the studies of multiple excitations. This issue is solved by the analytic con-

tinuation, which naturally introduces the concept of an effective fictitious bath. Second, we connect the steady-state quantum correlation functions of the weakly driven emitter with Green functions of the undriven case, based on a relation between the multiparticle scattering amplitudes and the steady state of the master equation as initially proposed in Refs. [63, 64].

In particular, to demonstrate quantum non-Hermitian phenomena, we focus on the quantum nature of light as indicated by the second-order correlation function $g^{(2)}(0) < 1$ of the driven emitter. We explicitly identify the role of non-Hermiticity by establishing the relation

$$g^{(2)}(0) = \left| \frac{1}{1 - U\Pi_f(2\omega_d)} \right|^2, \quad (2)$$

where ω_d is the driving frequency, U is the strength of the nonlinear interaction, and the function Π_f is directly related to Green functions determined by non-Hermitian Hamiltonians. This allows us to show how the sub-Poissonian photon statistics despite weak nonlinearity results from the non-Hermitian part of the Hamiltonian.

Applying the above formalism, we predict the FQZ effect, where the spontaneous emission rate γ_n of n excitations ($n = 1, 2, \dots$) in emitters scales with the bath dissipation rate Γ as

$$\gamma_n \propto \Gamma^{-\nu_n}, \quad (3)$$

where the exponent $\nu_n < 1$. Equation (3) indicates that the decay rate is suppressed by strong dissipation, similarly as the well-known QZ effect (see, e.g., Refs. [69–78]), but the algebraic scaling here has the fractional exponent, differently from the characteristic featureless Γ^{-1} scaling of the QZ effect. Moreover, the scaling behavior of γ_n varies with the number n of excitations, which can be controlled via the detuning of the emitter.

The physical picture for the FQZ effect is the following. When the open bath is strongly dissipative by itself, the emitters are dynamically imposed to mainly couple with the long-lived bath modes hosted near the dissipation band edge [Fig. 1(b)]. The dDOS of this region then determines the scaling behaviors of the emitters: Whenever the dDOS there diverges, fractional scaling arises as in Eq. (3), regardless of whether γ_k is gapless or not. The scaling analysis for the open bath with arbitrary dissipation band structure and dimension is summarized in Table I (see Sec. VII).

Specifically, for a single excitation, we identify the long-lived quasibound state as the superposition of the emitter excitation and the bosonic modes of the open bath, whose decay rates as given by Eq. (3) determine the emitter dynamics at long times (see Fig. 3 and Sec. VA 1). The bath modes in the quasibound state are confined to the dissipation band edge, forming a giant cloud around the emitters. The spatial size of the cloud grows with the bath dissipation rate Γ through a nonanalytic scaling. Consequently, when two emitters are present, the open bath mediates simultaneous sizable and remote quantum correlations of emitters, with

a correlation length increasing with Γ . These results are shown in Fig. 4 and Sec. V A 2.

For two excitations with nonlinear interactions, we find the emergence of quasibound states with the FQZ scaling $\nu_2 < \nu_1 < 1$. For instance, $\nu_1 = 1/2$ and $\nu_2 = 1/3$ for single and two excitations indicates a much faster spontaneous decay of two excitations compared to a single excitation. Moreover, the scalings can be independently controlled via the emitter detuning and the nonlinear interaction. These results are summarized in Fig. 5 and Sec. V B.

As a remarkable manifestation of FQZ effect, we show it opens a new route toward the generation of strong antibunching, even in the limit of weak interactions [Figs. 1(c) and 6]. By using Eq. (2) to analyze $g^{(2)}(0)$ of a single emitter under a weak driving field, we find significant antibunching behavior of excitations (see Sec. VI). We show how it results from the appropriately engineered $\gamma_1 < \gamma_2$, enabled by the independently controllable, different FQZ effects of one and two excitations. In particular, we can achieve strong antibunching in the weak-interaction regime $U/2 < 2\gamma_1 < \gamma_2$, even when interactions are so small as $U/2 < \gamma_1$.

The FQZ-induced antibunching originates from the structured dissipation of the open bath and, therefore, is conceptually different from the conventional mechanisms including strong nonlinearities [42] and interferences [43, 44]. Notably, it represents a first genuine quantum phenomenon emerging from non-Hermitian bands.

Our results have important implications for advancing the field of non-Hermitian physics into fully quantum regimes. Despite significant interest and ongoing efforts, state of the art experiments (see, e.g., Refs. [11, 13–15, 17, 18, 20–23]) on non-Hermitian phenomena in quantum systems have been limited to classical or single-particle physics. Theoretically (see, e.g., Refs. [25–29]), it remains an open challenge to explicitly show quantum many-body phenomena purely governed by a non-Hermitian Hamiltonian in the full quantum dynamics including quantum jumps, without conditioning on the measurements such as postselections. Our work sheds light on how to surmount these challenges.

III. EMITTERS COUPLED TO AN OPEN BATH

In this section, we describe in detail the theoretical model for the emitters coupled to a 1D open bath and outline the key quantities we are interested in.

Our setup in Fig. 1(a) consists of three ingredients: emitters a (blue ball), a bath of bosonic modes b (gray), and an auxiliary bath of lossy modes c (yellow). (i) We consider the paradigm of one and two emitters. In the rotating frame with respect to the central frequency of b

modes, the Hamiltonian of emitters is written as

$$H_{\text{emit}} = \sum_{l=1,2} \left[\left(\Delta a_l^\dagger a_l + \frac{U}{2} a_l^{\dagger 2} a_l^2 \right) + \varepsilon (a_l^\dagger e^{-i\omega_d t} + \text{H.c.}) \right], \quad (4)$$

where Δ is the detuning of emitters. The second term is the on-site Kerr interaction with strength U , which, in the limits $U \rightarrow 0$ and $U \rightarrow \infty$ describes a free boson mode and a two-level system, respectively. The third term describes the driving field with amplitude ε and driving frequency ω_d . (ii) The free propagation of the bosonic mode b in a lattice of N_b sites is described by the tight-binding Hamiltonian $H_b = \sum_{j=1}^{N_b} (J e^{i\theta} b_j^\dagger b_{j+1} + \text{H.c.})$ with the hopping strength J and the nontrivial phase $\theta \neq 0$, where b_j (b_j^\dagger) is the annihilation (creation) operator at site j . (iii) Finally, the lossy modes c_j ($j = 1, \dots, N_b - 1$) have the common decay rate $\gamma_c/2$.

We assume that the coupling of emitters to local modes $b_{j=0,d}$ is described by the Jaynes-Cummings (JC) Hamiltonian $H_{\text{sb}} = \Omega (a_1 b_0^\dagger + a_2 b_d^\dagger + \text{H.c.})$ with a Rabi frequency Ω . As shown in (i) in Fig. 1(a), neighboring modes b_j and b_{j+1} are both coupled to the mode c_j with a coupling strength g , described by $H_{\text{bc}} = g \sum_j (b_j^\dagger + b_{j+1}^\dagger) c_j + \text{H.c.}$

When the decay rate $\gamma_c/2$ of the bath c is much larger than all the other energy scales, it can be adiabatically eliminated [79, 80] to yield a master equation for the reduced density matrix ρ associated with the hybrid system that consists of the emitters and the bath b , i.e.,

$$\partial_t \rho = -i[H_{\text{emit}} + H_{\text{sb}} + H_b, \rho] + \mathcal{D}_b[\rho]. \quad (5)$$

Here, the dissipator takes the form

$$\mathcal{D}_b[\rho] = -\{H_D, \rho\} + \Gamma \sum_j \left(b_{j+1} \rho b_j^\dagger + b_j \rho b_{j+1}^\dagger + 2b_j \rho b_j^\dagger \right), \quad (6)$$

where $H_D = \Gamma \sum_j [(b_j^\dagger b_{j+1} + \text{H.c.})/2 + b_j^\dagger b_j]$ with the effective decay rate $\Gamma = 4g^2/\gamma_c$. The dissipator \mathcal{D}_b leads to a dissipative coupling rate $\Gamma/2$ between neighboring bath modes b_j and b_{j+1} in the lattice on top of the coherent coupling rate J , along with an on-site decay rate Γ of b_j . We note that dissipatively coupled lattices have been recently engineered with atoms [17, 18] and photonic resonators [21]. Subsequently, we denote the effective non-Hermitian Hamiltonian of Eq. (5) by $H_{\text{eff}} = H_{\text{emit}} + H_{\text{sb}} + H_b - iH_D$.

Thus, the master equation (5) describes a scenario where quantum emitters are coupled to an “open bath” b , which undergoes dissipation by itself as governed by the dissipator \mathcal{D}_b , apart from its own coherent evolution as governed by H_b . Competition of this two processes is characterized by the ratio $\Gamma/(2J)$. In the limit of $\Gamma/(2J) \rightarrow 0$, the traditional closed bath is recovered [45–48], whereas, in the opposite limit of $\Gamma/(2J) \gg 1$, the bath is dominated by its open nature.

Our goal is to study the spontaneous emissions of multiple excitations in emitters and the dynamics of quan-

tum correlation functions. We specifically consider two paradigmatic cases.

(i) We first consider the case without the driving field ($\varepsilon = 0$), and the emitter a_1 is initially populated with one and two excitations, while the bath b is initially in the vacuum state. We study the spontaneous emissions of excitations at times $t > 0$ characterized by

$$\begin{aligned} G(t) &= -i\langle 0|a_l(t)a_1^\dagger(0)|0\rangle, \\ D(t) &= -i\frac{1}{2}\langle 0|a_1^2(t)a_1^{\dagger 2}(0)|0\rangle, \end{aligned} \quad (7)$$

with $l = 1, 2$, where the average is taken on the vacuum state $|0\rangle$.

(ii) We then consider a single emitter a_1 driven by a weak field ($\varepsilon \neq 0$). We analyze the statistics of the emitter excitations in the steady state, as quantified by the second-order correlation function

$$g^{(2)}(\tau) = \frac{1}{n^2} \text{Tr} \left[a_1^\dagger a_1^\dagger(\tau) a_1(\tau) a_1 \rho_{\text{ss}} \right] \quad (8)$$

with $n = \text{Tr}(a_1^\dagger a_1 \rho_{\text{ss}})$ being the first-order correlation function, in the steady state ρ_{ss} of the master equation (5). Whenever $g^{(2)}(0) < 1$, the statistics is sub-Poissonian [42], which is genuine quantum statistics with no classical analogs.

IV. FORMALISM

In this section, we systematically develop an efficient approach based on the Keldysh formalism and the scattering theory to solve for the dynamics and quantum correlation functions of the weakly driven and nonlinear emitters. In particular, it allows us to identify purely non-Hermitian scenarios. In principle, for small systems, the master equation (5) can be solved numerically. However, to access the dynamical long-time behaviors of the highly nonlinear, driven emitters in the thermodynamic limit $N_b \rightarrow \infty$ requires intensive numerical calculations based on the finite-size scaling. Moreover, while the emitter and the open bath as a whole undergoes Markovian time evolution described by the master equation, we remark that the dynamics of the emitter, by itself, is non-Markovian because of the structured dispersion and dissipation of the open bath, and a successive elimination of the bath b from Eq. (5) to obtain a master equation for the emitters is not valid.

Our approach to obtain the full dynamics of emitters hinges on two important elements. (i) In the master equation (5) without driving ($\varepsilon = 0$), the action of the jump operator depletes the excitations from the open bath, but the effective Hamiltonian H_{eff} commutes with the number operator $N = \sum_l a_l^\dagger a_l + \sum_j b_j^\dagger b_j$, and, therefore, the steady state is the vacuum state. Consequently, the spontaneous emission dynamics of n ($n = 1, 2, \dots$) excitations is fully captured by the n -particle retarded Green function in the vacuum state. In Secs. IV A—IV C,

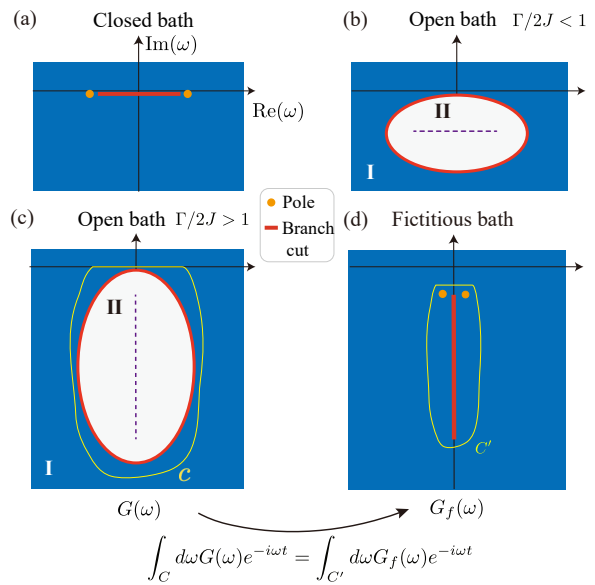


Figure 2. Illustration of the concept of the formalism for emitters in the open bath. The illustrated bath has the complex energy spectrum $\epsilon_k - i\gamma_k$, with $\epsilon_k = 2J \sin k$ and $\gamma_k = \Gamma(1 + \cos k)$, for $k \in (-\pi, \pi]$. (a)—(c) Distinct analytical structures of the Green function $G(\omega)$ in the complex frequency plane $\omega = \text{Re}(\omega) + i\text{Im}(\omega)$, when the bath is (a) closed, (b) open with $\Gamma/(2J) < 1$, and (c) open with $\Gamma/(2J) > 1$. In (a), the orange dots denote the poles of $G(\omega)$, representing the bound states, and the red line denotes the branch cut $\in [-2J, 2J]$, representing the scattering continuum. In (b) and (c), the red ellipses denote the branch cut parametrized by (ϵ_k, γ_k) , whose major axis is denoted by the dashed line. The self-energy (11) obtained from the residue theorem [81] is $\Sigma(\omega) = 0$ in region II (white) but is finite in region I (blue). Regions I and II are separated by the branch cut. The emitter dynamics is $G(t) = \int_C (d\omega/2\pi) G(\omega) e^{-i\omega t}$ with an integration along a contour C (yellow curve) in I. (d) Concept of the fictitious bath. We use the analytical continuation [81] to construct a fictitious bath with a simple spectrum, which generates the same emitter dynamics. The associated Green function $G_f(\omega)$ has a line branch cut (red line) and two poles (yellow dots), so $G(t) = \int_{C'} (d\omega/2\pi) G_f(\omega) e^{-i\omega t}$ can be efficiently calculated. This concept is applicable for multiple excitations and wide parameter regimes from $\Gamma/(2J) \ll 1$ to $\Gamma/(2J) \gg 1$.

we develop the formalism for undriven emitters coupled to the open bath. (ii) When emitters are weakly driven ($\varepsilon \neq 0$), although the steady state of the master equation is out of equilibrium, which violates the dissipation-fluctuation theorem, we are able to connect the correlation functions of the weakly driven emitter with Green functions of the undriven case following the spirit of Refs. [63, 64], as described in Sec. IV E. Detailed derivations in our formalism can be found in Appendixes A and B.

A. Non-Hermitian emitter-bath Hamiltonian

Without the driving field ($\epsilon = 0$), at zero temperature the steady state of the master equation (5) is the vacuum state $|0\rangle$. In the vacuum state, the time-ordered single-particle Green functions $G^t(t) = -i\langle 0|\mathcal{T}a_l(t)a_1^\dagger(0)|0\rangle$ and the retarded Green functions $G^R(t) = -i\langle 0|[a_l(t), a_1^\dagger(0)]|0\rangle$ coincide with each other, i.e., $G^t(t) = G^R(t) \equiv G(t)$. As a result, in the frequency domain, all the emitter Green functions in the single-excitation subspace are determined by $G(\omega) = \langle 0|a[1/(\omega - H_{\text{eff}})]a^\dagger|0\rangle$. In general, in the vacuum state, all the emitter Green functions in the n -excitation subspace are determined by the retarded n -particle ($n = 1, 2, \dots$) Green function. Hereupon, we drop “retarded” for convenience.

Thus, the dynamics of undriven emitters is purely governed by the effective emitter-bath Hamiltonian H_{eff} (see also Appendix B), which in the momentum space is written as

$$H_{\text{eff}} = H_a + \sum_k (\epsilon_k - i\gamma_k) b_k^\dagger b_k + \frac{\Omega}{\sqrt{N_b}} \sum_k (a_1^\dagger + a_2^\dagger e^{ikd}) b_k + \text{H.c.} \quad (9)$$

with $b_k = (1/\sqrt{N_b}) \sum_j b_j e^{-ikj}$ ($k \in (-\pi, \pi]$). In Eq. (9), the second term is the non-Hermitian Hamiltonian describing the open bath, which exhibits structured dispersion relation $\epsilon_k = 2J \cos(k + \theta)$ and dissipation rate $\gamma_k = \Gamma(1 + \cos k)$. It is easy to check that $[H_{\text{eff}}, N] = 0$ with $N = \sum_l a_l^\dagger a_l + \sum_k b_k^\dagger b_k$; i.e., the number of excitations is a good quantum number. In subsequent discussions, we assume $\theta = -\pi/2$ without loss of generality.

B. Property of the Green function associated with the open bath

To derive the dynamics of undriven emitters, we obtain the single-particle Green function $G(\omega)$ analytically by integrating out bath modes b . For instance, for a single emitter, we obtain

$$G(\omega) = \frac{1}{\omega - \Delta - \Sigma(\omega)} \quad (10)$$

which is determined by the self-energy

$$\Sigma(\omega) = \Omega^2 \int \frac{dk}{2\pi} \frac{1}{\omega - \epsilon_k + i\gamma_k}. \quad (11)$$

One can then further obtain the two-particle Green function

$$D(\omega) = \frac{1}{\Pi^{-1}(\omega) - U} \quad (12)$$

with $\Pi(\omega) = i \int d\omega' G(\omega') G(\omega - \omega') / (2\pi)$. The general expression of Green functions for many emitters is derived in Appendix A.

As a reference point, let us first recall how to obtain the emitter dynamics in a closed bath where $\gamma_k = 0$. There, it follows from the Lehmann spectral representation $G(\omega) = \int_{-\infty}^{\infty} \mathcal{A}(x) / (\omega - x + i0^+) dx$ that the emitter dynamics is determined by the analytic structure of the Green function $G(\omega)$ in the complex ω plane shown in Fig. 2(a). There, two isolated poles ϵ_s [i.e., $G^{-1}(\epsilon_s) = 0$] correspond to the energies of bound states, and the branch cut $x \in [-2J, 2J]$ represents the continuum of the bath, i.e., the scattering states. Thus, $G(\omega)$ in the entire complex plane is determined only by the nonzero spectral weight $\mathcal{A}(x)$ in the vicinity of poles and branch cut that can be obtained straightforwardly [81]. Based on the Lehmann representation, the Fourier transform of $G(\omega)$ can be obtained efficiently; the contribution from poles leads to the long-term oscillation of the remnant excitation in the emitter, while depending on the energy dispersion of the bath, the branch cut gives rise to (non-)Markovian decay [e.g., the power-law (exponential) decay $\sim 1/t^\delta$ ($e^{-\gamma t}$)].

For the open bath, however, the momentum-dependent decay rate $\gamma_k \neq 0$ generally leads to nontrivial and rich analytic structure of $G(\omega)$. As illustrated in Figs. 2(b) and 2(c), according to Eq. (11), the branch cut deforms from the structureless straight line to an ellipse (ϵ_k, γ_k) (red curve) parametrized by k . It separates the first Riemann surface (RS) to two disconnected regions: The self-energy is $\Sigma(\omega) = 0$ in the white region ($\omega \in \text{II}$) but finite in the blue region ($\omega \in \text{I}$). Depending on the ratio $\Gamma/(2J)$, the elliptical branch cut undergoes an interesting deformation [Figs. 2(b) and 2(c)]: Its major axis (dashed line) shrinks from a line on the real axis for $\Gamma/(2J) < 1$ to a point for $\Gamma/(2J) = 1$ and then expands in the orthogonal direction in the negative imaginary axis for $\Gamma/(2J) > 1$.

When $G(\omega)$ exhibits a branch circle, the two-particle Green function (12) contains an even more complicated analytic structure consisting of a “branch area.” As such, the computation of emitter dynamics is nontrivial, where it is generally hard to perform the Fourier transform (yellow curve) and the convolution directly.

C. Efficient solution via a fictitious bath

In order to efficiently solve the emitter dynamics, we introduce the “fictitious bath”: As we prove, an appropriate *fictitious bath* with a *simple* spectrum

$$\bar{\omega}_k = \begin{cases} -i\Gamma - 2J_{\text{eff}} \sin k, & \text{for } \Gamma/2J < 1 \\ -i\Gamma - 2iJ_{\text{eff}} \cos k, & \text{for } \Gamma/2J > 1 \end{cases} \quad (13)$$

with $J_{\text{eff}} = \sqrt{|J^2 - \Gamma^2/4|}$ generates exactly the *same* dynamics of the emitters [Fig. 2(d)].

The dispersion (13) of the fictitious bath is obtained using the analytic continuation, as illustrated in Figs. 2(c) and 2(d), which allows one to collapse the complex elliptical branch cut to a line coinciding with its major

axis. Mathematically, the Fourier transforms $F(t) = \int_C (d\omega/2\pi) F(\omega) e^{-i\omega t}$ ($F = G, D$) are integrals along the yellow contour C in region I, which is not contractible due to the elliptical branch cut in the first RS. However, it turns out that the self-energy $\Sigma(\omega)$ can be properly defined in the second RS by analytic continuation (see Appendix A). As an example, for one emitter, in region II of the first RS and region I of the second RS, $\Sigma(\omega) \equiv \Sigma_f(\omega)$ is unified as

$$\Sigma_f(\omega) = \Omega^2 \int \frac{dk}{2\pi} \frac{1}{\omega - \bar{\omega}_k}. \quad (14)$$

The advantage of the analytic continuation is that one can further deform the integral contour C to C' (yellow curve) in the second RS.

Thus, the emitter dynamics is completely determined by the fictitious bath

$$F(t) = \int_{C'} \frac{d\omega}{2\pi} F_f(\omega) e^{-i\omega t} \quad (15)$$

for ($F = G, D$) through the simple analytic structure of $G_f(\omega) = 1/(\omega - \Delta - \Sigma_f)$ and $D_f(\omega) = [\Pi_f^{-1}(\omega) - U]^{-1}$ with $\Pi_f(\omega) = i \int d\omega' G_f(\omega') G_f(\omega - \omega') / (2\pi)$. Figure 2(d) showcases the significantly simplified analytical structure of the Green function $G_f(\omega)$ associated with the fictitious bath. There, two poles $\bar{\epsilon}_s$ (orange dots) and a branch cut $\bar{\omega}_k$ (red line) remarkably connect two foci of the original elliptical branch cut of $G(\omega)$ in the original model. The spectral weights $\bar{Z}_s^{-1} = 1 - \partial_\omega \Sigma_f|_{\omega=\bar{\epsilon}_s}$ and $\mathcal{A}(x)$ of poles and the branch cut can be obtained analytically, giving rise to single- and two-excitation dynamics described by $G(t)$ and $D(t)$, respectively [81].

The fictitious-bath approach can be applied to efficiently compute the dynamics of multiexcitations or multiple emitters in a generic 1D open bath in the thermodynamic limit. We emphasize, however, that the bath dynamics, e.g., the multiexcitation scattering off the emitter and the propagation in the bath, *cannot* be studied via the fictitious bath.

Interestingly, the spectrum $\bar{\omega}_k$ of the fictitious bath in Eq. (13) coincides with that of the original bath under open boundary conditions (OBCs) in the thermodynamic limit. It is worth noting that the original open bath under OBCs exhibits a skin effect [2]. In contrast, the effective Hamiltonian of the fictitious bath exhibits completely different eigenstates, without a skin effect.

D. Dissipative density of states

In the context of closed baths with structured energy dispersions ϵ_k , the energy density of states (DOS) of the bath has played an important role in the emitter-bath interaction. For an open bath with also structured dissipation described by γ_k , analogously, we introduce dDOS labeled by $D_s(\gamma)$, namely, the number of bath modes

with a dissipation rate γ . The 1D dDOS is defined as

$$D_s(\gamma) := \int \frac{dk}{2\pi} \delta(\gamma - \gamma_k). \quad (16)$$

Explicit calculation of Eq. (16) leads to Eq. (1). In Sec. VII, we introduce dDOS in arbitrary dimensions and analyze the behavior of the self-energy through dDOS for arbitrary open baths with strong dissipations.

E. Second-order correlation function of a weakly driven emitter

We turn to calculate the steady-state correlation functions of an emitter a driven by a weak field with frequency ω_d . By weak, we mean the driving strength ε is finite but much smaller than the spectral gap of the system without the driving field. In the presence of driving ($\varepsilon \neq 0$), the steady state of Eq. (5) is nonequilibrium, for which the dissipation-fluctuation theorem no longer holds. However, we can connect the steady-state correlation functions with the Green function of the undriven case.

Such a connection is enabled by a relation between scattering and the master equation formalism as first proposed in Ref. [63], where the intuitive picture is the following: In the weakly driven system, the driving field just pumps the system by injecting multiple photons; thus, the pumping process can be considered as the few-photon scattering off an undriven system. This idea has been successfully applied to many quantum optical systems [64, 82, 83]. Here, we follow the similar spirit, as detailed in Appendix B.

In particular, we obtain the first- and second-order correlation functions of the weakly driven emitter in terms of Green functions of the undriven case as

$$\begin{aligned} \frac{\langle a^\dagger a \rangle_{\text{ss}}}{\varepsilon^2} &= \left| \int_{-\infty}^{\infty} dt e^{-i\omega_d t} \langle 0 | \mathcal{T} a(0) a^\dagger(t) | 0 \rangle \right|^2 \\ \frac{\langle a^\dagger a^\dagger(\tau) a(\tau) a \rangle_{\text{ss}}}{\varepsilon^4} &= \left| \int_{-\infty}^{+\infty} dt_1 dt_2 e^{-i\omega_d(t_1+t_2)} G(\tau; t_1, t_2) \right|^2 \end{aligned}$$

with $G(\tau; t_1, t_2) = -i \langle 0 | \mathcal{T} a_1(\tau) a_1(0) a_1^\dagger(t_1) a_1^\dagger(t_2) | 0 \rangle / 2$. Here, $a(t) = e^{iH_{\text{eff}}^\dagger t} a e^{-iH_{\text{eff}} t}$ is governed by the non-Hermitian Hamiltonian (9) without driving.

As the key result, by applying the Dyson expansion to calculate Green functions of the undriven emitter (see Fig. 11, Appendix A), we obtain

$$g^{(2)}(\tau) = |1 + \bar{\Pi}_f(\tau) T(2\omega_d)|^2, \quad (17)$$

with the scattering matrix $T(2\omega_d) = [U^{-1} - \Pi_f(2\omega_d)]^{-1}$ and the two-particle Green function

$$\bar{\Pi}_f(\tau) = i \int \frac{d\omega'}{2\pi} G_f(\omega_d + \omega') G_f(\omega_d - \omega') e^{-i\omega' \tau}.$$

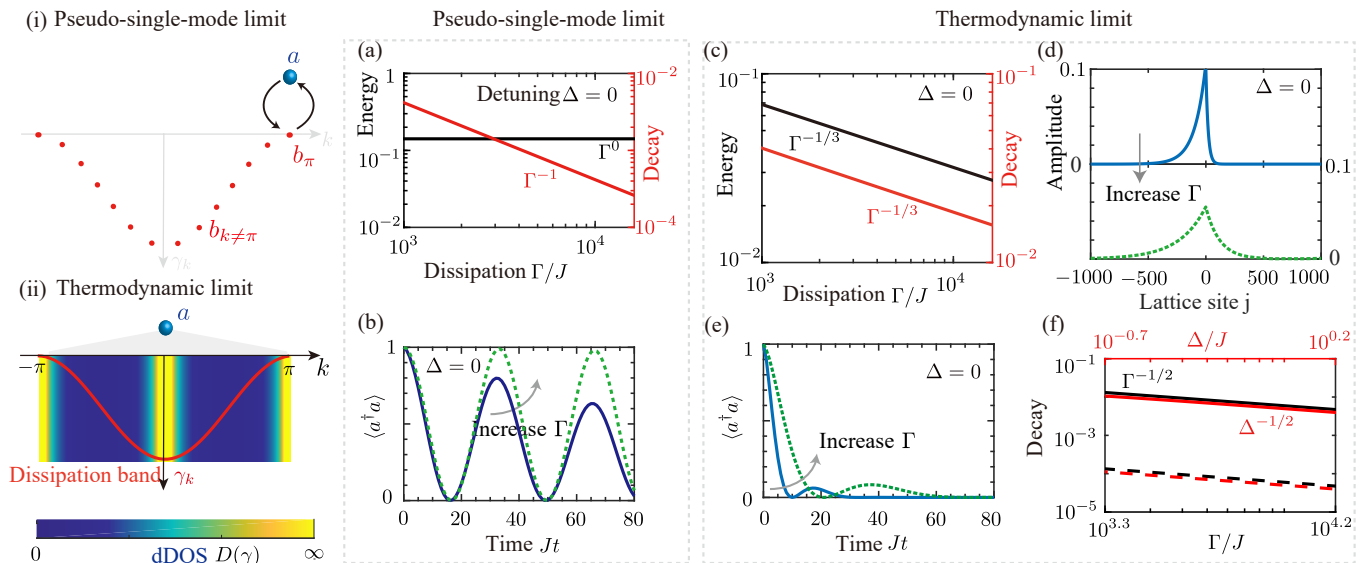


Figure 3. Spontaneous emission of an emitter with single excitation in a strongly dissipative open bath. Left [(i),(ii)]: physical picture. (i) Pseudo-single-mode regime: In a finite-size bath, the gap in the dissipation spectrum (red dots) isolates the long-lived bath mode b_π from $b_{k \neq \pi}$. Eliminating $b_{k \neq \pi}$ yields an effective model where the emitter a (blue ball) couples only to b_π . (ii) Thermodynamic limit: Because of divergent dDOS (1) (colored square) at $k = \pi$ of the dissipation band γ_k (red curve), the emitter couples strongly to the dissipation band edge. Center [(a),(b)]: QZ effect in the pseudo-single-mode regime. (a) Scalings with the bath dissipation Γ/J . By diagonalizing the Hamiltonian (9) with the Rabi frequency $\Omega/J = 1$, size $N_b = 50$, and detuning $\Delta = 0$, we find two eigenstates agreeing with that of the effective model in (i). The (positive) energy and decay rate are shown as a function of Γ/J . (b) Population dynamics $\langle a^\dagger(t)a(t) \rangle$. Numerical results are obtained using Eq. (9) with $\Omega/J = 0.3$ and $N_b = 10$, for $\Gamma/J = 20, 500$ (solid and dashed line, respectively). Right [(c)–(f)]: FQZ effect in the thermodynamic limit. (c) Scaling behavior of the quasibound states when $\Delta = 0$. By numerically solving the poles of the function $G_f(\omega)$ using Eq. (18) with $\Omega/J = 1$, we show the (positive) energy and decay rate of the quasibound state as a function of Γ/J . (d) Giant quasibound state. Its wave function is found by diagonalizing Eq. (9) with $N_b = 2000$, $\Delta = 0$, and $\Omega/J = 1$. The amplitude of its bath component at lattice site $j \in [-1000, 1000]$ is shown for $\Gamma/J = 100, 1000$ (solid and dashed line, respectively). (e) Population dynamics $\langle a^\dagger(t)a(t) \rangle = |G(t)|^2$ when $\Delta = 0$. Here, $G(t)$ is obtained from the numerical Fourier transform of $G_f(\omega)$ with $\Omega/J = 1$ and $\Gamma/J = 100, 1000$ (solid and dashed line, respectively). (f) Scaling behavior of the quasibound state when $\Delta \neq 0$. By numerically solving the poles of $G_f(\omega)$ with $\Omega/J = 1, 0.1$ (solid and dashed line, respectively), we plot the decay rate of the quasibound state, whose energy is Δ , as a function of Γ (black line) for $\Delta/J = -0.7$ and a function of Δ (red line) for $\Gamma/J = 10000$, respectively. (a), (c), and (f) are double-log plots. In (b) and (e), the initial conditions are $\langle a^\dagger(0)a(0) \rangle = 1$ and the vacuum state of the bath.

In the asymptotic limit $\tau \rightarrow \infty$, $g^{(2)}(\infty) \rightarrow 1$ as $\bar{\Pi}_f(\tau)$ tends to zero. In the limit $\tau \rightarrow 0$, we obtain $g^{(2)}(0)$ in Eq. (2) from the identity $\bar{\Pi}_f(0) = \Pi_f(2\omega_d)$.

Since $g^{(2)}(0) < 1$ indicates the quantum nature of light, Eqs. (2) and (17) provide us the central principle to explicitly identify the role played by the non-Hermiticity of the effective Hamiltonian in generating sub-Poissonian quantum light.

We emphasize that the formalism developed in this section is general, applicable for arbitrary non-Hermitian band structures $\epsilon_k - i\gamma_k$ of the bath.

V. FRACTIONAL QUANTUM ZENO EFFECT

Based on the above formalism, in this section, we explore the emitter physics in the strong dissipation regime $\Gamma/(2J) \gg 1$, for $\epsilon_k = 2J \sin k$ and $\gamma_k = \Gamma(1 + \cos k)$, and reveal the FQZ effects for different numbers of excita-

tions. Cases for the open bath with arbitrary forms of dissipation bands and dimensions are discussed in Sec. VIII.

A. Single excitation

We begin with studying the dynamics in the single-excitation subspace, where the on-site interaction U does not play any role and the non-Hermitian emitter-bath Hamiltonian (9) becomes quadratic. We consider the cases with one and two emitters, respectively.

1. Single emitter

When the open bath is dominated by its intrinsic dissipation for $\Gamma/(2J) \gg 1$, vital for the emitter dynamics at long times are bath modes with small dissipation rates. To gain intuitions into the physics, let

us first consider a bath with the finite size N_b and, thus, a discrete dissipation spectrum [Fig. 3(i)], where there opens a gap $\delta\gamma = 2\pi^2\Gamma/N_b^2$ between the mode b_π with $\gamma_k = 0$ and the rest modes $b_{k\neq\pi}$. Under the condition $\Omega/\delta\gamma \ll 1$, the fast-decaying modes $b_{k\neq\pi}$ can be adiabatically eliminated in the lowest-order perturbation treatment, yielding an effective Hamiltonian $H_{\text{eff}} = \Omega(a_1^\dagger b_\pi + b_\pi^\dagger a_1)/\sqrt{N_b} + (\Delta - i\gamma_1)a_1^\dagger a_1$. It describes that the emitter, which has the effective decay rate $\gamma_1 \approx (\Omega^2/N_b\Gamma) \sum_{k\neq\pi} 1/(1+\cos k) \propto \Gamma^{-1}$ (i.e., standard QZ effect), is coupled to a single bath mode b_π with an effective coupling strength $\Omega/\sqrt{N_b}$. Thus, the emitter with $\Delta = 0$ is expected to undergo a Rabi oscillation at frequency $2\Omega/\sqrt{N_b}$, which is protected by the QZ effect. As such, we refer to the regime of $\Omega/\delta\gamma \ll 1$ as the pseudo-single-mode regime.

The above analysis for the finite-size limit is verified by numerical simulations using the original non-Hermitian Hamiltonian H_{eff} in Eq. (9) with a finite size N_b under the condition $\Omega/\delta\gamma \ll 1$. Specifically, we find two eigenstates of H_{eff} coincide with that of the above effective model, whose eigenvalues show the expected Γ^{-1} scaling [Fig. 3(a)]. The numerical result of time-dependent population $\langle a_1^\dagger(t)a_1(t) \rangle$ in Fig. 3(b) clearly shows QZ dynamics, where the strong bath dissipation constrains the emitter to a coherent evolution in the subspace of the emitter and the mode b_π .

However, in the thermodynamic limit [Fig. 3(ii)], the structured dDOS associated with the dissipation band, which diverges near the edge, invalidates the above single-mode picture. To reveal the resulting emitter dynamics, we employ the formalism developed in Sec. IV to obtain the self-energy [81]

$$\Sigma_f(\omega) = \frac{-i\Omega^2}{\sqrt{-(\omega + i\Gamma)^2 - 4J_{\text{eff}}^2}} \quad (18)$$

and the Green function $G_f(\omega) = 1/[\omega - \Delta - \Sigma_f(\omega)]$ associated with the fictitious bath. In the regime $\Gamma/(2J) \gg 1$, where the bath undergoes strong dissipation by itself, the contribution to the emitter dynamics from the branch cut is found to decay as $\sim e^{-\Gamma t}$ (see Appendix A). On the long times $Jt \gg 1/\Gamma$, as shown, the emitter dynamics is determined by the poles $\epsilon_s \equiv \epsilon_b - i\gamma_b$ of G_f , i.e., $G_f^{-1}(\epsilon_s) = 0$, where ϵ_b and γ_b represent the energy and the decay rate of the quasibound state, respectively. Interestingly, the quasibound states exhibit different behavior depending on the detuning Δ .

For zero detuning $\Delta = 0$, two quasibound state solutions

$$\epsilon_s \equiv \epsilon_b - i\gamma_b = \frac{1}{2} \left(\pm\sqrt{3} - i \right) \left(\frac{\Omega^4}{2} \right)^{1/3} \Gamma^{-1/3} \quad (19)$$

exhibit the same nonanalytic scalings with Γ , in both the energy and the decay rate. Thus, the quasibound state displays the FQZ effect. Note that $\epsilon_b/\gamma_b = \sqrt{3}$ is a constant. Equation (19) is confirmed by the numerical solutions of $G_f^{-1}(\epsilon_s) = 0$ in Fig. 3(c).

The long-lived quasibound state is a superposition of the emitter and the bosonic modes of the open bath, i.e., $|B\rangle = c_1 a_1^\dagger |0\rangle + \sum_k f_k b_k^\dagger |0\rangle$, where c_1 and f_k are the coefficients. As detailed in Appendix C, we find $f_k = c_1(\Omega/\sqrt{N_b})\{1/[\epsilon_s - (\epsilon_k - i\gamma_k)]\}$. According to Eq. (19), the average momentum of the bath component is *sharply* localized at $k_b \rightarrow \pi$, as indicated by the fact that $\epsilon_s \rightarrow 0$ for $\Gamma \rightarrow \infty$. In real space, the bath modes localized around the emitter form a giant cloud with a large localization length $l_b \propto (\Gamma/\Omega)^{2/3}$ [see Eqs. (C3)–(C6), Appendix C], which increases with Γ through a nonanalytic scaling. The giant size of the cloud as shown in Fig. 3(d) extends impressively over hundreds of lattice sites at large Γ . Note that the asymmetry is due to the asymmetry of the bath under $k \rightarrow -k$.

Thus, the emergence of the FQZ effect can be understood: The strong bath dissipation effectively tailors the coupling of emitter with the continuum to the dissipation-band edge near $k = \pi$; there, the divergent dDOS gives rise to a strong emitter-bath interaction, leading to the fractional scaling behavior of the emitter. Indeed, as we rigorously prove later in Sec. VII, the fractional scaling always emerges if the dDOS near the dissipation band edge diverges, irrespective of whether γ_k is gapless or not. This is in strong contrast to what happens in the closed-bath case, where the bound state is created if the emitter is on resonance with the edge of the energy band ϵ_k (in our case, this corresponds to the limit of $\Gamma \rightarrow 0$ and when tuning $\Delta \approx \pm 2J$ near resonance with the edge of $\epsilon_k = 2J \sin k$ at $k = \pm\pi/2$).

The excitation population $\langle a_1^\dagger(t)a_1(t) \rangle = |G(t)|^2$ on the emitter is determined by the Fourier transform of the Green function $G_f(\omega)$. In the long-term limit, the result [81]

$$G(t) \approx \frac{4}{3} e^{-\gamma_b t} \cos(\sqrt{3}\gamma_b t) \quad (20)$$

from the double-pole approximation represents the long-lived oscillation between two quasibound states. It indicates that both the revival time and the lifetime of the emitter become longer when Γ increases, while the maximum revival population is almost constant as a result of $\epsilon_b/\gamma_b = \sqrt{3}$. In Fig. 3(e), we show the dynamics of $\langle a_1^\dagger(t)a_1(t) \rangle$ obtained from the numerical Fourier transform of $G_f(\omega)$. It agrees with Eq. (20) very well at times $t > 1/\Gamma$.

For a finite detuning $\Delta \neq 0$, however, the two quasibound states show different scalings, i.e.,

$$\epsilon_s^{(1)} = \Delta - i \frac{\Omega^2}{\sqrt{2}\Delta} e^{i(\pi/4)} \Gamma^{-1/2}, \quad (21)$$

$$\epsilon_s^{(2)} = -i \left(\frac{\Omega^4}{2\Delta^2} + 2J^2 \right) \Gamma^{-1}. \quad (22)$$

The decay rate of the first quasibound state in Eq. (21) exhibits the FQZ scaling $\propto \Gamma^{-1/2}$, in contrast to the other one in Eq. (22) with the QZ scaling $\propto \Gamma^{-1}$. Interestingly, the former also scales fractionally as $\propto \Delta^{-1/2}$ with Δ . In

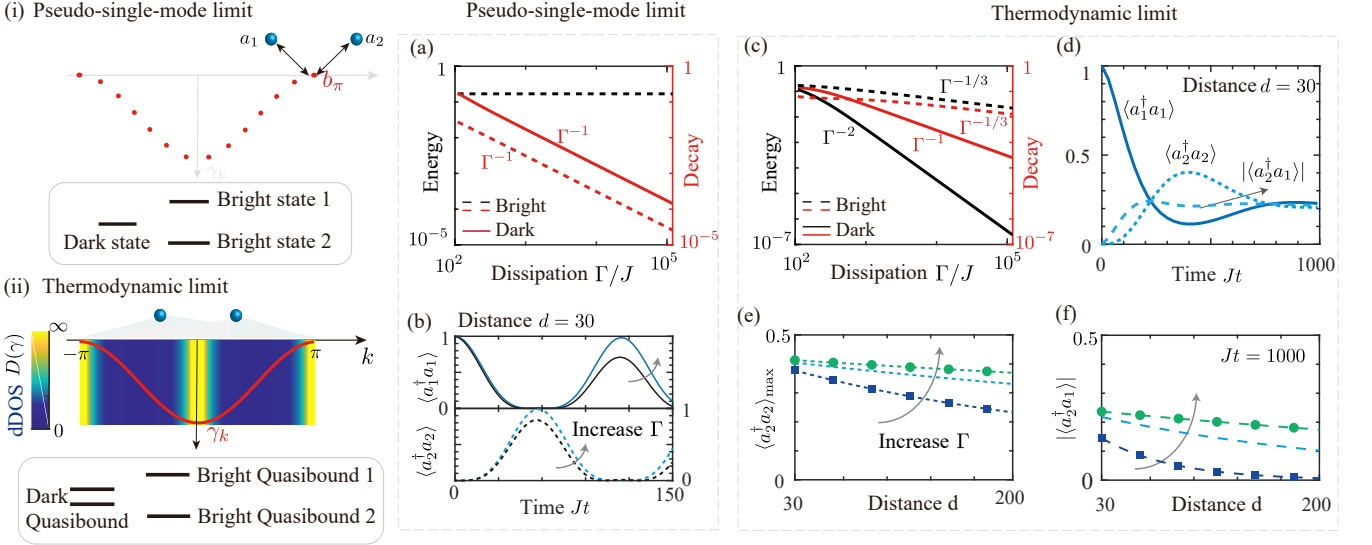


Figure 4. Remote state transfer and quantum correlation between two emitters mediated by a strongly dissipative open bath. Left [(i),(ii)]: physical picture. (i) Pseudo-single-mode regime: For a finite-size bath, elimination of bath modes $b_{k \neq \pi}$ yields an effective model where emitters a_1 and a_2 interact via a single mode b_π , forming a dark state and two bright states. (ii) Thermodynamic limit: Because of divergent dDOS (colored square) at $k = \pi$ of γ_k (red curve), two emitters interact strongly with the dissipation band edge, yielding two dark and two bright quasibound states. Center [(a),(b)]: QZ effect in the pseudo-single-mode regime. (a) Scaling with Γ/J . By diagonalizing Eq. (9) with Rabi frequency $\Omega/J = 1$ and $N_b = 70$ sites, we find a dark state (solid line) and two bright states (dashed line) described by the effective mode in (i). Their energy (black line) and decay rate (red line) are shown as a function of Γ/J . The energy of the dark state is approximately $10^{-15}J$ and negligible. (b) Population dynamics $\langle a_l^\dagger(t)a_l(t) \rangle$ ($l = 1, 2$). Results are numerically obtained using Eq. (9) with $\Omega/J = 0.3$ and $N_b = 60$, for $\Gamma/J = 500, 10000$ (black and blue line, respectively). Right [(c)–(f)]: FQZ effect in the thermodynamic limit. (c) Scaling behavior of the dark and bright quasibound states. By numerically solving the poles of $G_\pm(\omega)$ [81] using Eq. (23) with $\Omega/J = 1$ and distance $d = 30$, we plot the energy and decay rate as a function of Γ/J . (d) Dynamics of populations and correlations. Results are obtained via numerical Fourier transform of $G_\pm(\omega)$ with $\Omega/J = 0.3$ and $\Gamma/J = 40000$. (e) Maximum population $\langle a_2^\dagger a_2 \rangle_{\max}$ and (f) long-time quantum correlation $|\langle a_2^\dagger(t)a_1(t) \rangle|$ at $Jt = 1000$ as a function of d (even number), with $\Omega/J = 0.3$ and $\Gamma/J = 10000, 40000, 100000$ (square-dashed, dashed, and dot-dashed line, respectively). In (a)–(f), the detuning is $\Delta = 0$. In (b) and (d)–(f), the initial conditions are $\langle a_1^\dagger(0)a_1(0) \rangle = 1$, $\langle a_2^\dagger(0)a_2(0) \rangle = 0$, and the vacuum state of the bath. (a) and (c) are double-log plots.

Fig. 3(f), we present the numerical solutions for the decay rate of the first quasibound state, which confirm the predicted nontrivial scalings. The long-term dynamics of the emitter is primarily determined by Eq. (21), which indicates an oscillation with frequency Δ and a decay dynamics that can be fractionally suppressed via enhancing both Γ and Δ .

2. Two emitters

We now show that the FQZ effect leads to remarkable remote, long-term quantum correlation between two emitters. Tunable long-range correlation has been actively pursued in the closed-bath context such as using atoms coupled to a photonic crystal [37, 39, 58]. Therein, however, a trade-off exists between the correlation length and the correlation strength, because the increase of photonic localization length in the atom-photon bound state is accompanied with reduced atomic population. Here, we show that the strongly dissipative open bath can me-

diate simultaneous substantial and long-range quantum correlation, due to the formation of a dark quasibound state composed of two emitters and the bath component with a very large spatial size.

We focus on the interesting case $\Delta = 0$ and assume the distance d of two emitters to be an even number without loss of generality. Again, we start from the pseudo-single-mode regime [Fig. 4(i)] to gain some intuition. In this case, adiabatic elimination of the bath modes $b_{k \neq \pi}$ yields the effective non-Hermitian Hamiltonian $H'_{\text{eff}} = \sum_{l=1,2} [-i\gamma_l a_l^\dagger a_l + \Omega/\sqrt{N_b}(a_l^\dagger b_\pi + \text{H.c.})]$, where γ_1 is the same as before and $\gamma_2 \approx (\Omega^2/N_b\Gamma) \sum_{k \neq \pi} e^{-ikd}/(1 + \cos k)$. It describes a three-level system where two emitters are coupled to the bath mode b_π , protected by the standard QZ effect. In the limit $\Gamma/(2J) \rightarrow \infty$, the anti-symmetric superposition of two emitters in the odd channel forms a dark state $|\psi_-\rangle = (a_1^\dagger - a_2^\dagger)|0\rangle/\sqrt{2}$ decoupled from all bath modes, whereas in the even channel the symmetric superposition of emitters hybridizes with the b_π mode to form two bright states, $|\psi_+\rangle =$

$c_1(a_1^\dagger + a_2^\dagger)|0\rangle/\sqrt{2} + c_2 b_\pi^\dagger|0\rangle$, where c_1 and c_2 are coefficients. This physical picture indicates that, due to the dark state, excitation initially populating the first emitter is transferred to the second emitter at some time $t < \Gamma^{-1}$ even when they are remotely separated.

In the thermodynamic limit, however, two emitters are strongly coupled to the dissipation band edge with divergent dDOS [Fig. 4(ii)]. For the separation d within the spatial size of the localized bath modes, analogy with the pseudo-single-mode case suggests potential creations of dark (bright) quasibound states in odd (even) channels.

Mathematically, we determine the energy and the decay rate of the two-emitter quasibound states from the poles of Green functions $G_\pm(\omega) = 1/(\omega - \Sigma_f^\pm)$ in the even (odd) channels $+$ ($-$), where the self-energies Σ_f^\pm are [81]

$$\Sigma_f^\pm(\omega) = -i \frac{\Omega^2[1 \pm z_+^d(\omega)]}{\sqrt{-(\omega + i\Gamma)^2 - 4J_{\text{eff}}^2}} \quad (23)$$

with $z_+(\omega) = i(\omega + i\Gamma)/2J_{\text{eff}} + \sqrt{-[(\omega + i\Gamma)^2/4J_{\text{eff}}^2] - 1}$. The approximate solution for the complex energy ϵ_s of the quasibound state can be obtained analytically via the Taylor expansion. For $\Omega/J > \sqrt{2/d}$, we find two solutions for the ‘‘dark’’ quasibound states

$$\epsilon_s = \pm R - id\Omega^2\Gamma^{-1} \quad (24)$$

in the odd channel with $R \sim \Gamma^{-2}$ and two solutions for the bright quasibound states in the even channel:

$$\epsilon_s = \frac{1}{2} \left(\pm\sqrt{3} - i \right) (2\Omega^4)^{1/3} \Gamma^{-1/3}. \quad (25)$$

The above results indicate that the decay rate of the dark quasibound state is controlled by the distance d and exhibits QZ scaling. Instead, the two bright quasibound states are blind to d and feature the FQZ scaling $\Gamma^{-1/3}$ the same as the single-emitter case, except that the prefactor is enhanced by a factor of $4^{1/3}$. These analytical results are confirmed by numerical solutions of the poles of the Green functions $G_\pm(\omega)$, as shown in Fig. 4(c). Note that the dark quasibound state relies on strong dissipation and divergent dDOS of the dissipation band edge; hence, it is different in nature from the bound states with small decay rates in the context of a closed bath with multiple emitters [57, 84], where the energy resonance mechanism plays a fundamental role.

According to Eqs. (23)–(25), the bright quasibound state of the complex energy ϵ_s exhibits the localization length $l_b \sim 1/\log[|z_+(\epsilon_s)|]$, which sets a characteristic length scale for the interaction of two emitters. Remarkably, $|z_+| \rightarrow 1$ in the limit $\Gamma/(2J) \rightarrow \infty$ indicates a remote correlation mediated by the bath mode near the dissipation-band edge, where the FQZ effect gives rise to a nonanalytic scaling of the correlation length $l_b \propto (\Gamma/\Omega)^{2/3}$ with Γ .

The dynamics of two emitters directly follows from the Fourier transforms $G_{1n}(t) \sim \int (G_+ \pm G_-) e^{-i\omega t} d\omega / (4\pi)$

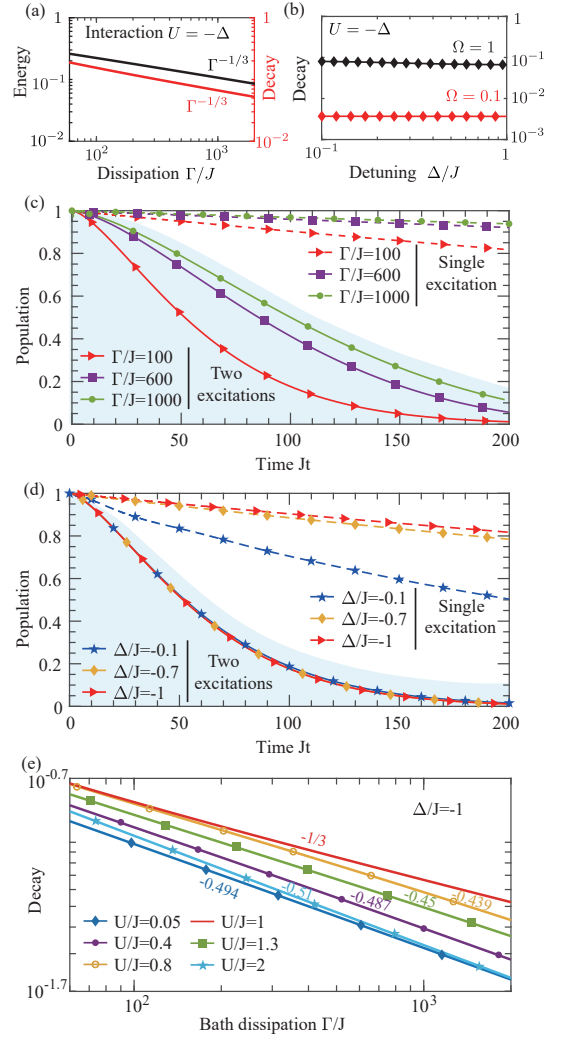


Figure 5. FQZ effect of two excitations in a nonlinear emitter and comparison with the single-excitation case. For two excitations, their interaction strength U and the detuning Δ satisfy $U = -\Delta$ in (a)–(d). All numerical results are obtained via the approach in Sec. IV. (a) Scalings of the energy (black line) and decay rate (red line) of the two-excitation quasibound states with the bath dissipation rate Γ . The Rabi frequency is $\Omega/J = 1$ and $\Delta/J = -1$. (b) Decay rate of the quasibound state as a function of Δ , when $\Gamma/J = 1000$ and $\Omega/J = 0.1, 1$ (red and black line, respectively). (a) and (b) are double-log plots. (c), (d) Comparisons between spontaneous emissions of single and two excitations, when (c) Γ is changed and $\Delta/J = -1$ and (d) Δ is changed and $\Gamma/J = 100$. In (c) and (d), $\Omega/J = 0.1$. (e) FQZ scaling $\Gamma^{-\nu}$ ($\nu < 1$) of two-excitation quasibound states for $U \neq -\Delta$, when $\Delta/J = -1$ and $\Omega/J = 1$. Beside each curve, the extracted value of $-\nu$ is labeled.

for $n = 1, 2$ as [81]

$$iG_{1n}(t) = \frac{2}{3} e^{-\bar{\gamma}t} \cos(\sqrt{3}\bar{\gamma}t) \pm \frac{1}{2} e^{-(\Omega^2 d/\Gamma)t}, \quad (26)$$

where $\bar{\gamma} = \Omega^{4/3}/(4\Gamma)^{1/3}$. In Fig. 4(d), we numerically perform the Fourier transforms to obtain the time-

dependent population $\langle a_n^\dagger(t)a_n(t) \rangle = |G_{1n}(t)|^2$ and the correlation $|\langle a_2^\dagger(t)a_1(t) \rangle|$ of two remote emitters separated by $d = 30$. The results at long times $t > 1/\Gamma$ agree very well with Eq. (26).

When $d/l_b \ll 1$, Eq. (26) predicts the maximal transferred population on the second emitter is $\langle a_2^\dagger a_2 \rangle_{\max} \rightarrow 0.36$ [Fig. 4(d)] at the time $t_s \sim \pi/(\sqrt{3}\bar{\gamma})$. When d increases, $\langle a_2^\dagger a_2 \rangle_{\max}$ diminishes [Fig. 4(e)] due to the increased decay rate of the dark quasibound state [see Eq. (24)]. However, as long as $d/l_b \ll 1$, the population decreases as $\propto -d/l_b$, leading to a state transfer that can occur across hundreds of lattice sites.

Interestingly, due to the presence of the dark quasibound state, a remote correlation $|\langle a_2^\dagger(t)a_1(t) \rangle| \sim 0.25$ between two emitters can exist for a remarkably long time, as expected from Eq. (26) under the condition $t < \Gamma/(d\Omega^2)$; see Fig. 4(d). The remoteness of the long-term correlation is showcased in Fig. 4(f). When $d < \Gamma/(1000\Omega^2)$, we see that the correlation diminishes linearly and slowly with d , remaining substantial over a distance $d \sim 200$ even at such a long time $Jt = 1000$. These results suggest the possibility to flexibly engineer simultaneous significant and remote correlations in practice where the finite-size bath is generally in between the thermodynamic and the quasi-single-mode limits.

B. Two excitations

In this section, we study the spontaneous emission of two excitations in an emitter with the on-site interaction U . We show that the decay rate of two excitations exhibits distinct FQZ scalings from the single-excitation counterpart, which can be tuned via U and Δ .

Since the effective emitter-bath Hamiltonian (9) commutes with N , we can expand it in the two-excitation subspace spanned by the basis $\{a_1^{\dagger 2}|0\rangle/\sqrt{2} \equiv |d\rangle, a_1^\dagger b_k^\dagger|0\rangle \equiv |k\rangle_e, b_k^\dagger b_{k'}^\dagger|0\rangle \equiv |kk'\rangle\}$. We obtain

$$\begin{aligned} H_2' &= (U + 2\Delta)|d\rangle\langle d| + \sum_k (\Delta + E_k)|k\rangle_e\langle k| \\ &+ \sum_k \frac{\sqrt{2}\Omega}{\sqrt{N_b}} (|k\rangle_e\langle d| + \text{H.c.}) + \sum_{kk'} (E_k + E_{k'})|kk'\rangle\langle kk'| \\ &+ \sum_{kk'} \frac{\sqrt{2}\Omega}{\sqrt{N_b}} (|k\rangle_e\langle kk'| + \text{H.c.}) \end{aligned} \quad (27)$$

where $E_k = \epsilon_k - i\gamma_k$ is the complex energy of the bath mode b_k .

Because the bath mode b_π has zero complex energy $E_\pi = 0$, Eq. (27) indicates two kinds of resonant processes. (i) For the interaction $U = -\Delta$, the doublon state $|d\rangle$ (i.e., two excitations in the emitter) is resonant with the state $|\pi\rangle_e$ (i.e., one excitation in the emitter and one excitation at $k = \pi$ in the bath). (ii) When $U = -2\Delta$, the resonant coupling occurs between the doublon state

$|d\rangle$ and the state $|\pi\pi\rangle$ (i.e., two excitations at $k = \pi$ in the bath).

It turns out that, in the resonant case $U = -\Delta$, the decay rates of two excitations have different scaling behaviors from the single-excitation sector. Under the condition $\Omega^2/\Delta\Gamma \ll 1$, the states $|kk'\rangle$ (i.e., two excitations in the bath) can be adiabatically eliminated (see Appendix C). To leading order, the dynamics is governed by the effective non-Hermitian Hamiltonian

$$H_2'' = \frac{\sqrt{2}\Omega}{\sqrt{N}} \sum_k (|k\rangle_e\langle d| + \text{H.c.}) + \sum_k E_k |k\rangle_e\langle k| \quad (28)$$

in the rotating frame, which is exactly the Hamiltonian in the *single-excitation* sector with $\Delta = 0$ and $\Omega \rightarrow \sqrt{2}\Omega$.

Equation (28) immediately allows us to use the earlier results of the single excitation to understand the physics of two excitations with the interaction $U = -\Delta$. Specifically, it indicates the existence of two giant two-excitation quasibound states whose complex energies are

$$\epsilon_s \equiv \epsilon_{b2} - i\gamma_{b2} = \frac{1}{2} (\pm\sqrt{3} - i) (2\Omega^4)^{1/3} \Gamma^{-1/3}. \quad (29)$$

We thus conclude that the spontaneous emission of two excitations is characterized by

$$D(t) \approx \frac{4}{3} e^{-\gamma_{b2}t} \cos(\sqrt{3}\gamma_{b2}t) \quad (30)$$

at long times, which exhibits the FQZ effect *without* explicit dependence on Δ and U .

To validate above analysis, we apply the approach in Sec. IV and derive the two-particle Green function $D_f(\omega) = [\Pi_f^{-1}(\omega) - U]^{-1}$ associated with the fictitious bath. By numerically solving the poles of $D_f(\omega)$, we find the energy and decay rate of two-excitation quasibound states under the condition $U = -\Delta$. The numerical results shown in Figs. 5(a) and 5(b) confirm the $\Gamma^{-1/3}$ scaling and the insensitivity to Δ . By numerically performing the transformation $D(t) = \int D_f(\omega) e^{-i\omega t} d\omega/2\pi$, we obtain the spontaneous emission of two excitations, as shown in Fig. 5(c) for various Γ and Fig. 5(d) for various Δ . These results clearly corroborate Eq. (30); in particular, variations in the finite detuning barely influence the emitter dynamics.

That the spontaneous emission rate of two excitations with interaction $U = -\Delta$ scales as $\Gamma^{-1/3}$ and is independent of Δ is in strong contrast to the single-excitation counterpart, where the decay rate scales as $\Gamma^{-1/2}$ and can be controlled by Δ [cf. Eq. (21) and Fig. 3(f)]. As shown in Fig. 5(c), the single excitation undergoes a significantly slower decay compared to two excitations. The large difference between the decay rates of one and two excitations is even more dramatic in Fig. 5(d). There, increasing Δ further suppresses the single-excitation decay as $\Delta^{-1/2}$, in contrast to the ‘‘frozen’’ evolution trajectory of two excitations.

For $U \neq -\Delta$, the fractional scalings appear generically; see Fig. 5(e) for $\Delta/J = -1$. Since in the non-interacting limit two excitations exhibit similar scaling

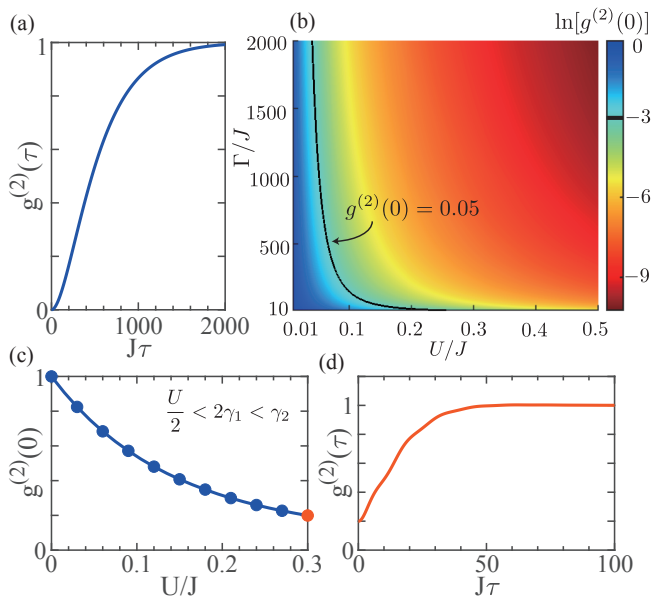


Figure 6. The FQZ-induced antibunching in a driven emitter. (a) Second-order correlation function $g^{(2)}(\tau)$ as a function of time τ . We calculate $g^{(2)}(\tau)$ in Eq. (8) based on Eq. (17), with the interaction $U/J = -\Delta/J = 0.3$ and the bath dissipation rate $\Gamma/J = 1000$. The driving frequency is $\omega_d/J = -0.303$. (b) Minimal $g^{(2)}(0)$ in the parameter spaces of interaction U/J and dissipation Γ/J when $U/J = -\Delta/J$. Calculations are based on Eq. (2). The black curve denotes where $g^{(2)}(0) = 0.05$. In (a) and (b), the JC coupling strength is $\Omega/J = 0.3$. (c),(d) Strong antibunching in the weak-interaction regime $U/2 < 2\gamma_1 < \gamma_2$. (c) Minimal $g^{(2)}(0)$ as a function of interaction U . (d) $g^{(2)}(\tau)$ for $U/J = 0.3$ and $\omega_d/J = -0.42$. In (c) and (d), we use $\Gamma/J = 38.8$, $\Omega/J = 0.79$, and $\Delta/J = -0.3$.

behaviors as the single excitation, we anticipate the FQZ scaling to cross over from $\Gamma^{-1/2}$ to $\Gamma^{-1/3}$ when the interaction is tuned from $U = 0$ to $U = -\Delta$, as observed in Fig. 5(e).

Intriguingly, the *independently tunable* FQZ scalings for different numbers of excitations points to the possibility to tailor the emitter dynamics into the desired excitation subspaces. For instance, we can engineer the detuning $\Delta = -U$ and bath dissipation Γ in such a way that the two excitations decay much faster than the single excitation. This has the direct consequence of the hierarchical Zeno effect; namely, any weak pump field cannot populate the two-excitation subspace in the characteristic timescale $\sim \Gamma^{1/2}$, leading to confined dynamics in the single-excitation subspace.

VI. FQZ-INDUCED ANTIBUNCHING

In this section, we study the statistics of emitter excitations in the presence of a weak driving field. As predicted in Sec. VB, due to the FQZ effect, the dynamics

is expected to be frozen in the single-excitation subspace even with a weak nonlinearity. Conventionally, the strong single-photon nonlinearity relies on strong Kerr interactions [42] or interference [43, 44]. Here, we show that the FQZ effect presents a new mechanism in the limit of weak interactions.

Consider the driving light is on resonance with the single excitation, i.e., $\omega_d = \text{Re}[\epsilon_s^{(1)}]$. It is instructive to first obtain some estimation for the second-order correlation $g^{(2)}(\tau)$ in Eq. (17) in the regime $\Gamma/J \gg 1$. Assuming the approximation $G_f(\omega) \sim 1/(\omega - \epsilon_s^{(1)})$ [85], which leads to $\bar{\Pi}_f(\tau) \sim e^{-i(\epsilon_s^{(1)} - \omega_d)\tau}/[2(\omega_d - \epsilon_s^{(1)})]$, the resulting analytical expression reads

$$g^{(2)}(\tau) \sim \left| 1 + \frac{C e^{-i(\epsilon_s^{(1)} - \omega_d)\tau}}{1 - C} \right|^2. \quad (31)$$

The ratio $C = U/[2(\omega_d - \epsilon_s^{(1)})]$, as a figure of merit, determines the statistics of the emitter excitations. For $\Delta \neq 0$, we obtain from Eq. (21) that $C = iU\sqrt{|\Delta|}\Gamma/\Omega^2$, and Eq. (31) suggests $g^{(2)}(0) \sim 1/(1 + |C|^2) < 1$.

As an example, we analyze the photon statistics in the case $U = -\Delta$, where the decay rate $\gamma_2 \sim \Gamma^{-1/3}$ of two excitations is larger than that $\gamma_1 \sim \Gamma^{-1/2}$ of the single excitation. In the limit $|C| \gg 1$, Eq. (31) reduces to

$$g^{(2)}(0) \sim \frac{\Omega^4}{U^3\Gamma} \ll 1, \quad (32)$$

which indicates the sub-Poissonian statistics. The result (32) explicitly provides the scaling of $g^{(2)}(0)$ on Ω , U , and Γ . In addition, $g^{(2)}(\tau)$ saturates to unity in the timescale $\tau = 1/\gamma_1 = 1/\text{Im}[\epsilon_s^{(1)}]$. The condition (32) can be understood using an intuitive picture: As the decay rate of two excitations is $\sim \Omega^{4/3}\Gamma^{-1/3}$ [see Eq. (29)], the condition (32) indicates the interaction U is stronger than the two-excitation decay rate suppressed by the FQZ effect.

Figures 6(a) and 6(b) numerically validate the strong antibunching when $U = -\Delta$. There, the Rabi coupling $\Omega/J = 0.3$ is fixed, and the driving light is on resonance, i.e., $\omega_d = \text{Re}[\epsilon_s^{(1)}]$. In Fig. 6(a) for $\Gamma/J = 10^3$ and $U/J = -\Delta/J = 0.3$, the numerical result of $g^{(2)}(\tau)$ explicitly displays the antibunching behavior. In Fig. 6(b), we plot the numerical values of $g^{(2)}(0)$ in the Γ - U plane for $U = -\Delta$. As shown by the black curve, to realize a desired $g^{(2)}(0) = 0.05$, the required nonlinearity U becomes weaker as Γ increases, and in the large Γ limit $U \sim \Gamma^{-1/3}$, confirming the analysis based on Eq. (32).

When $U \neq -\Delta$, remarkably, capitalizing on the rich controllability over the FQZ scalings and, thus, the decay rates in different excitation subspaces, strong antibunching arises even for sufficiently weak nonlinearity $U/2 < 2\gamma_1 < \gamma_2$, as numerically shown in Fig. 6(c). This can be understood by noting that, without the nonlinearity U , the decay rates of the two excitations have the same scaling relation as the single excitation, i.e., $\gamma_2 = 2\gamma_1 \sim (|\Delta|\Gamma)^{-1/2}$. When increasing U to the resonant point $-\Delta$, however, the two-excitation decay rate

is gradually enhanced to $\gamma_2 \sim \Gamma^{-1/3}$ (see Fig. 5). In the crossover regime $0 < U < -\Delta$, therefore, one expects antibunching even in the weak nonlinearity regime $U/2 < 2\gamma_1 < \gamma_2$. In Fig. 6(c), we show sub-Poissonian statistics, i.e., $g^{(2)}(0) < 1$, for $\Gamma/J = 38.8$, $\Omega/J = 0.79$, and $\Delta/J = -0.3$, where $g^{(2)}(0)$ monotonically decays to 0.2 in the weak nonlinearity regime $U/2 < 2\gamma_1$. In Fig. 6(d), $g^{(2)}(0) < g^{(2)}(\tau)$ unambiguously displays antibunching behavior. We remark that the ability to engineer $\gamma_2 > 2\gamma_1$ due to the FQZ hierarchy allows for $g^{(2)}(0) < 0.5$ even when the interaction is so small as $U/2 < \gamma_1$. This cannot be accessed through the featureless QZ effect, where $\gamma_2 \approx 2\gamma_1$ results in $g^{(2)}(0) > 0.5$ for $U/2 < 2\gamma_1$.

VII. SCALING BEHAVIORS FOR THE ARBITRARY OPEN BATH

In previous sections, we illustrate the FQZ effect for the 1D open bath with $\gamma_k = \Gamma(1 + \cos k)$, which is gapless. To further understand the physics of the FQZ effect, we now present a general scaling analysis for the open bath with arbitrary dissipative bands $\gamma(\mathbf{k})$ in dimensions $d = 1, 2, 3$. As we show, the FQZ effect generically occurs as the result of strong dissipation and divergent dDOS near dissipative band edges, regardless of whether the bath spectrum is gapless or not. This makes the present fractional scaling intrinsically different from the conventional nonanalytic phenomena for which gapless modes are crucial.

Without loss of generality, we concentrate on the purely dissipative open bath [i.e., $\epsilon(\mathbf{k}) = 0$]. In general, the dissipative band $\gamma(\mathbf{k})$ has three characteristics. (i) The minimum dissipation rate is $\gamma_{\min} \equiv \min[\gamma(\mathbf{k})]$, which necessarily sits at the dissipation band edge with the quasimomentum \mathbf{k}_0 . When $\gamma_{\min} \neq 0$, it provides the dissipative gap of the open bath. (ii) For a spatially homogeneous bath, the dissipative dispersion near the dissipative gap (edge) at \mathbf{k}_0 can be approximated as

$$\gamma(\mathbf{k}) = \gamma_{\min} + c\Gamma|\mathbf{k} - \mathbf{k}_0|^\mu. \quad (33)$$

Here, the power μ depends on the specifics of $\gamma(\mathbf{k})$, the coefficient c is such that $c\mathbf{k}^\mu$ is dimensionless, and Γ characterizes the dissipation bandwidth. (iii) The dDOS in d dimensions is defined as

$$D_s(\gamma) := \int \frac{d^d k}{(2\pi)^d} \delta[\gamma - \gamma(\mathbf{k})]. \quad (34)$$

According to Eq. (33), the dDOS near γ_{\min} is given by

$$D_s(\gamma) = \frac{A}{(2\pi)^d} \frac{(\gamma - \gamma_{\min})^{-1+(d/\mu)}}{\mu(c\Gamma)^{d/\mu}}, \quad (35)$$

where the coefficient A depends on the dimensions. We immediately see that the dDOS near γ_{\min} diverges when $d/\mu < 1$ but vanishes when $d/\mu > 1$.

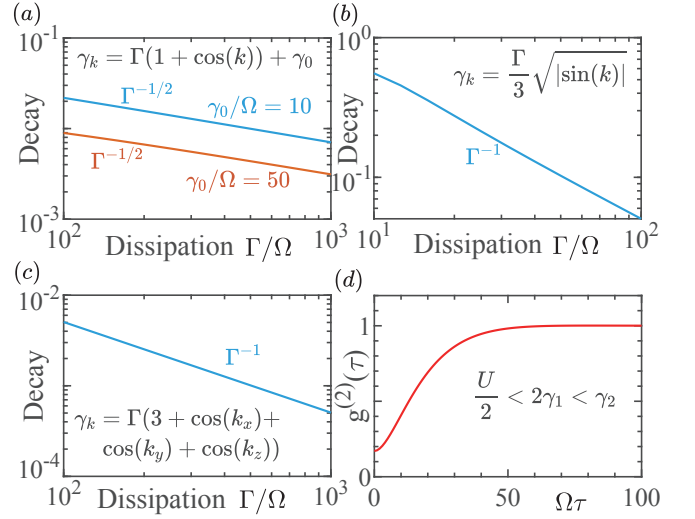


Figure 7. Scaling behavior of the emitter for various forms of $\gamma(\mathbf{k})$ and dimension of a purely dissipative bath. (a) $\gamma(k) = \gamma_0 + \Gamma(1 + \cos k)$, for $\gamma_0/\Omega = 10, 50$, respectively, (b) $\gamma(k) = (\Gamma/3)\sqrt{|\sin(k)|}$, and (c) $\gamma(\mathbf{k}) = \Gamma(3 + \cos k_x + \cos k_y + \cos k_z)$. (d) FQZ-induced antibunching in a gapped bath with $\gamma(k) = \gamma_0 + \Gamma(1 + \cos k)$. In (a)–(c), we take $\Delta = 0$. In (d), we choose $\Delta/\Omega = -0.2$, $\Gamma/\Omega = 25$, interaction $U/\Omega = 0.2$, $\gamma_0/\Omega = 5$, and $\omega_d/\Omega = -0.23$, and $J = 0$.

Now consider an emitter coupled with the open bath as before, and we are interested in the scaling behaviors of the complex energy ϵ_s of the quasibound states. We illustrate our analysis for $\Delta = 0$ and single excitation. By extending the formalism in Sec. IV to the d -dimensional bath, we aim to solve $s + \Sigma(s) = 0$, where $s = -i\omega$ and the self-energy reads as

$$\Sigma(s) = \Omega^2 \int \frac{d^d k}{(2\pi)^d} \frac{1}{s + \gamma(\mathbf{k})}. \quad (36)$$

Since relevant for the long-time dynamics are the bath modes in the vicinity of γ_{\min} , we use Eq. (33) to obtain

$$\begin{aligned} \Sigma &= \frac{A\Omega^2}{(2\pi)^d} \frac{1}{\mu(c\Gamma)^{d/\mu}} \int_{\gamma_{\min}}^{\Lambda} \frac{1}{s + \gamma} \frac{1}{(\gamma - \gamma_{\min})^{1-(d/\mu)}} d\gamma \\ &= C \left(\frac{\Lambda'}{\Gamma} \right)^{d/\mu} \frac{1}{s'} F \left(1, \frac{d}{\mu}, \frac{d}{\mu} + 1; -\frac{\Lambda'}{s'} \right). \end{aligned} \quad (37)$$

Here, we introduce a cutoff Λ and redefine $s' = s + \gamma_{\min}$ and $\Lambda' = \Lambda - \gamma_{\min} \propto \Gamma$. Moreover, $F(\alpha, \beta, \zeta; z)$ is the hypergeometric function, and the coefficient C depends on the dimensions. When the dissipation scale Γ is largest compared to all the other relevant energy scales, we can expand the self-energy (37) in terms of the small parameter $|s'/\Lambda'|$. We refer to Appendix D for detailed analysis.

At the leading order, we find (i) fractional scaling, $\Sigma \propto \Gamma^{-d/\mu}$ for $d/\mu < 1$, (ii) logarithmic behavior, $\Sigma \propto (\ln \Gamma)/\Gamma$ for $d/\mu = 1$, and (iii) integer scaling, $\Sigma \propto \Gamma^{-1}$ for $d/\mu > 1$. Finally, by solving $s + \Sigma(s) = 0$, we analytically derive the scaling relations for the complex

Table I. Scaling analysis of the complex energy ϵ_s of the longest-living quasibound state for an arbitrary open bath in d dimension. C is a general notation for prefactor.

| d/μ | dDOS | Gapped open bath ($\gamma_{\min} \neq 0$) | Gapless open bath ($\gamma_{\min} = 0$) |
|---------------------|---|---|---|
| $\frac{d}{\mu} < 1$ | $\lim_{\gamma \rightarrow \gamma_{\min}} D_s(\gamma) = +\infty$ | $\Delta + C(\gamma_{\min} - i\Delta)^{-1+(d/\mu)}\Gamma^{-d/\mu}$ | $\begin{cases} C\Gamma^{\frac{1-2\mu/d}{\mu}} & (\Delta = 0) \\ \Delta + C(-i\Delta)^{-1+(d/\mu)}\Gamma^{-d/\mu} & (\Delta \neq 0) \end{cases}$ |
| $\frac{d}{\mu} = 1$ | $\lim_{\gamma \rightarrow \gamma_{\min}} D_s(\gamma) = \text{Const} \neq 0$ | $\Delta - iC\Gamma^{-1} \ln(\frac{\Gamma}{\gamma_{\min}})$ | $\Delta - iC\Gamma^{-1} \ln(\frac{\Gamma}{\epsilon})$ |
| $\frac{d}{\mu} > 1$ | $\lim_{\gamma \rightarrow \gamma_{\min}} D_s(\gamma) = 0$ | $\Delta - iC\Gamma^{-1}$ | $\Delta - iC\Gamma^{-1}$ |

energy ϵ_s of quasibound states. The scalings for $\Delta \neq 0$ are obtained in a similar way.

In Table I, we collect the results of ϵ_s of the quasibound states with the smallest decay rate, for $\gamma_{\min} \neq 0$ and $\gamma_{\min} = 0$, respectively. We see that fractional scalings always arise whenever $D_s(\gamma_{\min}) \rightarrow \infty$, whereas the standard QZ effect emerges if $D_s(\gamma_{\min}) \rightarrow 0$. Note that, although singular dDOS may appear at other places of the Brillouin zone, in the strong dissipation regime, only the dDOS near γ_{\min} is important for the dynamical long-time behaviors of the emitters.

To validate above analysis, we numerically solve the poles of the single-particle Green function for three examples of $\gamma(\mathbf{k})$. The results for $\Delta = 0$ are presented in Fig. 7. The first example is $\gamma(k) = \gamma_0 + \Gamma(1 + \cos k)$, corresponding to the gapped version of the 1D case considered in previous sections. If gapless modes are necessary for the fractional scalings, one would expect the FQZ effect to disappear. Instead, in Fig. 7(a), we find the FQZ effect under various gap sizes of γ_0 , where the $\Gamma^{-1/2}$ scaling agrees with what is predicted from the quadratic dissipative dispersion $\gamma(k) = \gamma_0 + \Gamma(k - \pi)^2/2$ with the divergent dDOS at γ_0 . As the second example, we consider a gapless 1D dissipation band $\gamma(k) = \Gamma\sqrt{|\sin(k)|}/3$. We see that standard QZ effect emerges [Fig. 7(b)]. This can be understood, because $\gamma(k) \propto |k|^{1/2}$ near $\gamma_{\min} = 0$, so that the dDOS vanishes at $k = 0$, leading to the linear scaling according to Table I. The third example is $\gamma(\mathbf{k}) = \Gamma(3 + \cos k_x + \cos k_y + \cos k_z)$ in 3D. Similarly as its 1D counterpart analyzed previously, this is a gapless spectrum with $\gamma(\mathbf{k}) \propto |\mathbf{k} - \pi|^2$ near $\gamma_{\min} = 0$ at $\mathbf{k} = (\pi, \pi, \pi)$. However, Fig. 7(c) reveals a completely different behavior from the 1D case, where the QZ effect, instead of the FQZ effect, emerges, due to the vanishing 3D dDOS at $\gamma_{\min} = 0$.

In summary, we arrive at the physical picture that the FQZ effect occurs whenever the open bath itself undergoes strong dissipation and $D_s(\gamma_{\min})$ diverges, irrespective of whether there are gapless modes or not. This conclusion is applicable also for the case with multiple excitations. As an application, in Fig. 7(d), we show the FQZ-induced strong photon antibunching for a weak nonlinearity when the bath has the gapped dissipation spectrum $\gamma(k) = \gamma_0 + \Gamma(1 + \cos k)$. Note that, as shown by Table I, manipulation of dDOS can tune the scaling behavior, e.g., from fractional scalings to logarithmic behavior or to integer scalings.

VIII. EXPERIMENTAL IMPLEMENTATION

Although the FQZ effect is predicted in the thermodynamic limit, it can be observed for the open bath with the finite size N_b , provided N_b and the system parameters are such that the condition $\Omega/\delta\gamma \gg 1$ with $\delta\gamma = 2\pi^2\Gamma/N_b^2$ is satisfied (see Appendix E). In this section, we present the microscopic setup for realizing the FQZ effect by using ultracold atoms in the state-dependent optical lattices, as schematically illustrated in Fig. 8. Recently, engineered lattice models with dissipative couplings have been demonstrated with the momentum-space lattice of cold atoms [18] as well as an ensemble of photonic resonators [21] or atomic spin waves [17] coupled to the auxiliary reservoir. Our implementation of the master equation (5) is in line with these experiments.

We encode the emitter a , the bath b , and the auxiliary bath c in three ground-state hyperfine levels of the bosonic atom, labeled as $|1\rangle$, $|2\rangle$, and $|3\rangle$, respectively.

(i) In state $|1\rangle$, atoms can undergo Feshbach resonance and realize the nonlinear term $(U/2)a^\dagger a^2$. To realize the driving field, we can prepare the atomic Bose-Einstein condensate (BEC) in another hyperfine state labeled by $|4\rangle$ and use the external laser field with frequency ω_d to induce the transition between $|4\rangle$ and $|1\rangle$. This implements the driving term $\epsilon a^\dagger e^{-i\omega_d t} + \text{H.c.}$, where ϵ is related to the mean-field wave function of the BEC.

(ii) In state $|2\rangle$, atoms are deeply trapped in the 3D optical lattice with N_b sites. For realizing the FQZ effect, the term $\sum_j J e^{i\theta} b_j^\dagger b_{j+1} + \text{H.c.}$ is not necessary, as shown previously. Note that, for general purpose, this term can be readily realized via a two-photon Raman transition between the adjacent lattice sites [86], where the phase θ is controlled via the relative phase of the coupling lasers. The term $\Omega a^\dagger b_0 + \text{H.c.}$ is implemented by using the laser to induce the transition between $|1\rangle$ and $|2\rangle$.

(iii) In state $|3\rangle$, atoms are free in the $y - z$ directions but are deeply trapped in a 1D optical lattice in the x direction, where the tunneling rate is ignorable. When atoms are excited to $|3\rangle$, they are quickly lost from the system in the $y - z$ directions with the loss rate $\gamma_c/2$. Both b_j and b_{j+1} are near-resonant coupled to c_j via lasers ($j = 1, \dots, N_b - 1$), with the coupling rate g . For large loss rate $\gamma_c/2$, modes c_j can be adiabatically eliminated to realize the nonlocal dissipator in Eq. (6) with $\Gamma = 4g^2/\gamma_c$. To observe the FQZ effect requires one to tune the parameters to satisfy $\Omega/\delta\gamma \gg 1$.

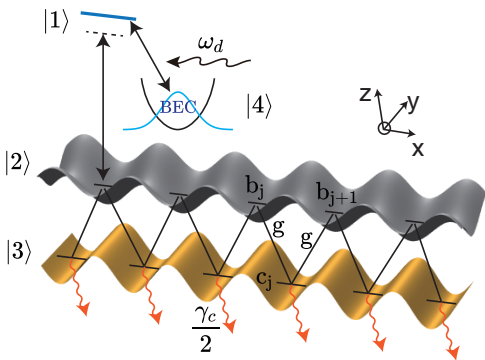


Figure 8. Implementation scheme with cold atoms for the master equation (5). We use three hyperfine levels of the bosonic atom, labeled as $|i\rangle$ ($i = 1, 2, 3$), respectively, to encode the emitter a , the bath b , and the auxiliary bath c . In $|1\rangle$, atoms can undergo Feshbach resonance. In $|2\rangle$, atoms are deeply trapped in the 3D lattice (gray). In $|3\rangle$, atoms are free in the $y - z$ directions but deeply trapped in a 1D optical lattice (orange) in the x direction. We prepare the atomic BEC in another hyperfine state labeled by $|4\rangle$ and use the laser with frequency ω_d to induce the transition between $|4\rangle$ and $|1\rangle$. States $|1\rangle$ and $|2\rangle$ are coupled by lasers. Both b_j and b_{j+1} are near-resonant coupled to c_j with the coupling rate g . When atoms are excited to $|3\rangle$, they are quickly lost from the system in the $y - z$ direction with a large loss rate $\gamma_c/2$.

An alternative atomic platform may be provided by thermal atoms in a vapor cell [14]. A unique feature of such setup is that atomic spin waves created by the electromagnetic-induced transparency in spatially separated optical channels is naturally dissipatively coupled via flying atoms. By further controlling the separation and laser beams, a dissipative atomic-spin-wave lattice has been realized [17]. The light interacting with the spin waves in an optical channel, thus, represents an emitter coupled to the open bath, whose properties can be detected via the transmission spectroscopy.

IX. CONCLUSION

In this work, we predict quantum non-Hermitian phenomena, the FQZ effect and the FQZ-induced sub-Poissonian photon statistics, based on a paradigm where nonlinear emitters interact with an engineered open bath. The FQZ effect generally arises from the combination of strong dissipation and divergent dDOS near the dissipation band edge and has no immediate counterpart in the closed-bath context. Capitalizing on its unique, excitation-number-dependent scaling behaviors, we are able to judiciously design a hierarchy of decay rates for the emitters. This opens a new route toward the generation of strong photon antibunching in the limit of weak nonlinearities. Remarkably, we identify that the present sub-Poissonian quantum statistics of photons is driven

by the key role of non-Hermiticity. Our result presents a first step toward the exploration of non-Hermitian quantum optics. It is also of relevance in the context of recent experiments for non-Hermitian lattice models, where demonstrating quantum non-Hermitian phenomena remains an open challenge.

Our work offers a new way to design the system-bath interaction by engineering the intrinsic dissipation band structure of the open bath. When the bath undergoes strong dissipation by itself, the emitters are dynamically enforced to mainly couple with the weakly dissipating modes hosted near the dissipation band edge, whose dDOS plays a central role in the dynamical long-time behaviors of emitters. This route complements the conventional way to engineer the emitter-bath interaction in the closed-bath context which crucially relies on the energy resonance. It also opens a new path to realize interesting quantum non-Hermitian physics, as well as quantum simulations of many-body systems. Beyond engineering either an energy or a dissipation band of the bath, it is interesting to explore how their combinations may give rise to intriguing quantum effects.

In summary, our work provides a feasible route in the highly desired, yet challenging, quest for non-Hermitian quantum many-body effects. Beyond the general fundamental interests, ultimately, understanding the role played by non-Hermiticity in fully quantum regimes will enable us to leverage recent advances in non-Hermitian Hamiltonian engineering for actual quantum applications.

X. ACKNOWLEDGEMENTS

We thank enlightening discussions with Carlos Navarette Benlloch, Hannes Pichler, Mikhail A. Baranov, Wei Yi, and Yanhong Xiao. This research is funded by National Key Research and Development Program of China (Grants No. 2022YFA1404201, No. 2022YFA1203903, and No. 2022YFA1404003), the National Natural Science Foundation of China (Grants No. 12034012 and No. 11874038), and NSFC-ISF (Grant No. 12161141018). T.S. is supported by National Key Research and Development Program of China (Grant No. 2017YFA0718304) and the National Natural Science Foundation of China (Grants No. 11974363, No. 12135018, and No. 12047503). Z.L. is supported by the National Natural Science Foundation of China (No. 52031014).

Y.S. and T.S. contributed equally to this work.

Appendix A: Green functions and analytic continuations

In this section, we derive the retarded Green functions $G^R(\omega)$ and $D^R(\omega)$ for the undriven emitters. By the ap-

appropriate analytic continuation, we introduce the Green function $G_f(\omega)$ also available in the second RS, which naturally gives rise to the effective Hamiltonian \bar{H}_{eff} describing emitters coupled to the bath with the simple dispersion relation and decay rates. In the first and second subsections, we study the situations for single and two emitters. In the third section, we derive $D^R(\omega)$ using the ladder diagram. The retarded Green function $D(t)$ in the time domain can be efficiently calculated using the analytic continuation $D_f(\omega)$ of $D^R(\omega)$.

Before proceeding, we remark that, at zero temperature, the steady state of the master equation (5) without the driving field ($\epsilon = 0$) is the equilibrium state represented by the vacuum state $|0\rangle$ of excitations. There, the fluctuation-dissipation theorem applies. Specifically, time-ordered single-particle Green functions $G^t(t) = -i\langle 0|\mathcal{T}a_l(t)a_1^\dagger(0)|0\rangle$ and the retarded Green functions $G^R(t) = -i\langle 0|[a_l(t), a_1^\dagger(0)]|0\rangle\theta(t)$ coincide with each other. Similarly, the time-ordered two-particle Green function $D^t(t) = -i\langle 0|\mathcal{T}a_1^2(t)a_1^{\dagger 2}(0)|0\rangle/2$ coincides with the retarded two-particle Green function $D^R(t) = -i\langle 0|[a_1^2(t), a_1^{\dagger 2}(0)]|0\rangle\theta(t)/2$. That is, $G^t(t) = G^R(t) \equiv G(t)$, and $D^t(t) = D^R(t) \equiv D(t)$, which have simple relations $G(t) = G^K(t)\theta(t)$ and $D(t) = D^K(t)\theta(t)$ with Keldysh Green functions $G^K(t) = -i\langle 0|\{a_l(t), a_1^\dagger(0)\}|0\rangle$ and $D^K(t) = -i\langle 0|\{a_1^2(t), a_1^{\dagger 2}(0)\}|0\rangle/2$, respectively. We show later in Appendix B 1 how one can efficiently study the spontaneous emission of n excitations ($n = 1, 2, \dots$) through the n -particle retarded Green function in $|0\rangle$.

1. Single emitter

For the open bath, the three Green functions, i.e., the retarded G_b^R , the advanced G_b^A , and the Keldysh G_b^K Green functions, in the frequency domain are

$$G_b(\omega) = \begin{pmatrix} G_b^K(\omega) & G_b^R(\omega) \\ G_b^A(\omega) & 0 \end{pmatrix} = \begin{pmatrix} \frac{-2i\gamma_k}{(\omega - \epsilon_k)^2 + \gamma_k^2} & \frac{1}{\omega - \epsilon_k + i\gamma_k} \\ \frac{1}{\omega - \epsilon_k - i\gamma_k} & 0 \end{pmatrix}$$

in the Keldysh space, where the dispersion relation $\epsilon_k = 2J \cos(k + \theta)$ and the decay rate $\gamma_k = \Gamma(1 + \cos k)$. As shown in Fig. 9, the Dyson expansion of the Rabi coupling term gives rise to the Green function

$$G(\omega) = \begin{pmatrix} G^K(\omega) & G^R(\omega) \\ G^A(\omega) & 0 \end{pmatrix} = \frac{1}{(\omega - \Delta)\sigma^x - \frac{\Omega^2}{N} \sum_k \sigma^x G_b \sigma^x}, \quad (\text{A1})$$

where σ^x is the Pauli matrix. More explicitly, the analytic structure of the retarded Green function

$$G^R(\omega) = \frac{1}{\omega - \Delta - \frac{\Omega^2}{N} \sum_k \frac{1}{\omega - \epsilon_k + i\gamma_k}}$$

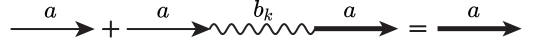


Figure 9. Feynman diagram for the single-excitation Green function. The thin (bold) arrow denotes the bare (exact) single-excitation Green function of the emitter, and the curvy line denotes the bare propagator of the bath mode.

fully determines the dynamics of the emitter. In the main text, we focus on the case $\theta = -\pi/2$.

Since the bath has the mode-dependent dispersion relation ϵ_k and decay rate γ_k , the branch cut $\omega_k = \epsilon_k - i\gamma_k$ forms an ellipse rather than collapsing into a line like that in the closed system ($\gamma_k = 0$). The ellipse centered at $(0, -\Gamma)$ has the major axis $2J$ and Γ for $2J > \Gamma$ and $2J < \Gamma$, respectively. In the special case $2J = \Gamma$, the branch cut becomes a circle. In the thermodynamic limit, the self-energy

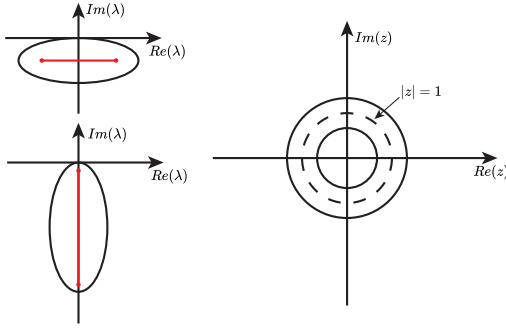
$$\Sigma(\omega) = \Omega^2 \int \frac{dk}{2\pi} \frac{1}{\omega - \omega_k} = \Omega^2 \int_{|z|=1} \frac{dz}{2\pi i z} \frac{1}{\omega - \lambda(z)}$$

becomes the contour integral in the z plane ($z = e^{ik}$), which is completely determined by the poles z_0 , i.e., $\omega - \lambda(z_0) = 0$, and the corresponding residues.

Before performing the lengthy calculation, we notice that the complex function $\lambda(z)$ conformally maps the annular region $1 < |z| < z_{\text{max}} = |[J + (\Gamma/2)]/[J - (\Gamma/2)]|$ into the inner region of the first RS, i.e., the region inside the ellipse, where, in particular, the contour $|z| = \sqrt{z_{\text{max}}}$ is mapped to a line connecting the foci of the ellipse (see Fig. 10). As a result, for ω localized inside the ellipse, the poles z_0 are always in the region $1 < |z| < z_{\text{max}}$, which results in the vanishing $\Sigma(\omega)$ in the first RS. The analytic continuation can be performed by the deformation of the integral contour from $|z| = 1$ to $|z| = \sqrt{z_{\text{max}}}$, which reproduces the same self-energy $\Sigma(\omega)$ in the first RS and extends it to the second RS. More specifically, for $2J > \Gamma$

$$\begin{aligned} & \Sigma_f(\omega) \\ &= \Omega^2 \int_{|z|=\sqrt{z_{\text{max}}}} \frac{dz}{2\pi i z} \frac{1}{\omega + i\Gamma - i(J - \frac{\Gamma}{2})z + i(J + \frac{\Gamma}{2})z^{-1}} \\ &= \Omega^2 \int_{|z|=1} \frac{dz}{2\pi i z} \frac{1}{\omega + i\Gamma - iJ_{\text{eff}}z + iJ_{\text{eff}}z^{-1}} \\ &= \Omega^2 \int \frac{dk}{2\pi} \frac{1}{\omega + i\Gamma + 2J_{\text{eff}} \sin k}, \end{aligned} \quad (\text{A2})$$

where $J_{\text{eff}} = \sqrt{J^2 - \Gamma^2/4}$ and in the last step we use the relation $z = e^{ik}$. The comparison between $\Sigma(\omega)$ and the last line in Eq. (A2) shows that the bath of the emitter can be effectively replaced by that with a much simpler spectrum $\bar{\omega}_k = -i\Gamma - 2J_{\text{eff}} \sin k$, where the decay rate is

Figure 10. Conformal map from the λ plane to the z plane.

the constant Γ . Similarly, for $2J < \Gamma$

$$\begin{aligned} & \Sigma_f(\omega) \\ &= \Omega^2 \int_{|z|=\sqrt{z_{\max}}} \frac{dz}{2\pi iz} \frac{1}{\omega + i\Gamma - i(J - \frac{\Gamma}{2})z + i(J + \frac{\Gamma}{2})z^{-1}} \\ &= \Omega^2 \int_{|z|=1} \frac{dz}{2\pi iz} \frac{1}{\omega + i\Gamma + iJ_{\text{eff}}z + iJ_{\text{eff}}z^{-1}} \\ &= \Omega^2 \int \frac{dk}{2\pi} \frac{1}{\omega + i\Gamma + 2iJ_{\text{eff}} \cos k}, \end{aligned}$$

where $J_{\text{eff}} = \sqrt{\Gamma^2/4 - J^2}$. For this case, the effective bath has the spectrum $\tilde{\omega}_k = -i\Gamma - 2iJ_{\text{eff}} \cos k$, where the dispersion relation becomes trivial.

The advantage of the analytic continuation is to collapse the complex elliptical branch cut to the line connecting the foci of the ellipse in the second RS. The contour integrals in $\Sigma_f(\omega)$ can be obtained efficiently as

$$\begin{aligned} \Sigma_f(\omega) &= \frac{\Omega^2 \text{sgn}[1 - |z_-(\omega)|]}{\sqrt{(\omega + i\Gamma)^2 - 4J_{\text{eff}}^2}}, \\ z_-(\omega) &= -i \left[\frac{\omega + i\Gamma}{2J_{\text{eff}}} - \sqrt{\frac{(\omega + i\Gamma)^2}{4J_{\text{eff}}^2} - 1} \right] \end{aligned}$$

for $2J > \Gamma$ and

$$\begin{aligned} \Sigma_f(\omega) &= \frac{i\Omega^2 \text{sgn}[1 - |z_-(\omega)|]}{\sqrt{-(\omega + i\Gamma)^2 - 4J_{\text{eff}}^2}}, \\ z_-(\omega) &= i \frac{\omega + i\Gamma}{2J_{\text{eff}}} - \sqrt{-\frac{(\omega + i\Gamma)^2}{4J_{\text{eff}}^2} - 1} \end{aligned}$$

for $2J < \Gamma$. The self-energy $\Sigma_f(\omega)$ results in the analytic continuation $G_f(\omega) = 1/[\omega - \Delta - \Sigma_f(\omega)]$ of $G^R(\omega)$.

The spontaneous decay of the excitation is described by the Fourier transform $G(t) = \int (d\omega/2\pi) e^{-i\omega t} G_f(\omega)$, which is determined by the behaviors in the vicinity of poles and branch cuts of G_f . For $2J > \Gamma$, the Green function

$$\begin{aligned} G_f(\omega) &= \sum_s \frac{Z_s}{\omega - \varepsilon_s} + \int_{-2J_{\text{eff}}}^{2J_{\text{eff}}} \frac{dx}{\pi} \frac{1}{\omega - x + i\Gamma} \\ &\times \frac{\Omega^2 \sqrt{4J_{\text{eff}}^2 - x^2}}{(4J_{\text{eff}}^2 - x^2)(x - \Delta - i\Gamma)^2 + \Omega^4} \end{aligned}$$

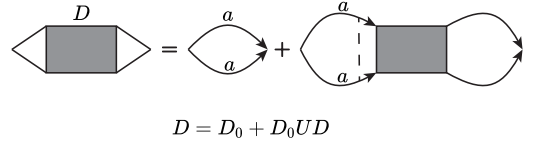


Figure 11. Feynman diagram for the two-excitation Green function. The first term is the convolution of two exact single-excitation Green functions. In the second term, the dashed line denotes the interaction of the emitter.

is determined by the poles ε_s [i.e., $G_f^{-1}(\varepsilon_s) = 0$], the corresponding residues

$$Z_s = \frac{1}{1 - \partial_\omega \Sigma_f|_{\omega=\varepsilon_s}}, \quad (\text{A3})$$

and the contribution from the branch cut, whose Fourier transform can be performed straightforwardly as

$$\begin{aligned} G(t) &= -i \sum_s Z_s e^{-i\varepsilon_s t} - i \int_{-2J_{\text{eff}}}^{2J_{\text{eff}}} \frac{dx}{\pi} \\ &\times \frac{\Omega^2 \sqrt{4J_{\text{eff}}^2 - x^2}}{(4J_{\text{eff}}^2 - x^2)(x - \Delta - i\Gamma)^2 + \Omega^4} e^{-ixt - \Gamma t}. \end{aligned}$$

For $2J < \Gamma$, the Fourier transform of the Green function

$$\begin{aligned} G_f(\omega) &= \sum_s \frac{Z_s}{\omega - \varepsilon_s} - \int_{-2J_{\text{eff}}}^{2J_{\text{eff}}} \frac{dx}{\pi} \frac{1}{\omega - ix + i\Gamma} \\ &\times \frac{\Omega^2 \sqrt{4J_{\text{eff}}^2 - x^2}}{(4J_{\text{eff}}^2 - x^2)(x - \Gamma + i\Delta)^2 + \Omega^4} \end{aligned}$$

gives

$$\begin{aligned} G(t) &= -i \sum_s Z_s e^{-i\varepsilon_s t} + i \int_{-2J_{\text{eff}}}^{2J_{\text{eff}}} \frac{dx}{\pi} \\ &\times \frac{\Omega^2 \sqrt{4J_{\text{eff}}^2 - x^2}}{(4J_{\text{eff}}^2 - x^2)(x - \Gamma + i\Delta)^2 + \Omega^4} e^{-(\Gamma-x)t}. \end{aligned} \quad (\text{A4})$$

2. Two emitters

For two emitters in the open bath, the retarded Green function

$$G^R(\omega) = \frac{1}{\omega - \Delta - \Sigma(\omega)}$$

of emitters is determined by the self-energy matrix $\Sigma(\omega)$ whose element is

$$\Sigma_{ll'}(\omega) = \frac{\Omega^2}{N} \sum_k \frac{e^{ik(l-l')}}{\omega - \varepsilon_k + i\gamma_k}. \quad (\text{A5})$$

In the thermodynamic limit, the matrix element becomes

$$\begin{aligned}
& \Sigma_{ll'}(\omega) \\
&= \Omega^2 \int \frac{dk}{2\pi} \frac{e^{ikd_{ll'}}}{\omega - \varepsilon_k + i\gamma_k} \\
&= \Omega^2 \int_{|z|=1} \frac{dz}{2\pi iz} \frac{z^{d_{ll'}}}{\omega - \lambda(z)} \\
&= \Omega^2 \int_{|z|=1} \frac{dz}{2\pi iz} \frac{z^{d_{ll'}}}{\omega + i\Gamma - i(J - \frac{\Gamma}{2})z + i(J + \frac{\Gamma}{2})z^{-1}},
\end{aligned}$$

where $d_{ll'} = l - l'$.

The analytic continuation can also be applied here as

$$\begin{aligned}
& \Sigma_{f, ll'}(\omega) \\
&= \Omega^2 \int_{|z|=\sqrt{z_{\max}}} \frac{dz}{2\pi iz} \frac{z^{d_{ll'}}}{\omega + i\Gamma - i(J - \frac{\Gamma}{2})z + i(J + \frac{\Gamma}{2})z^{-1}} \\
&= \Omega^2 z_{\max}^{d_{ll'}/2} \int_{|z|=1} \frac{dz}{2\pi iz} \frac{z^{d_{ll'}}}{\omega + i\Gamma - iJ_{\text{eff}}z + iJ_{\text{eff}}z^{-1}} \\
&= \Omega^2 z_{\max}^{d_{ll'}/2} \int \frac{dk}{2\pi} \frac{e^{ikd_{ll'}}}{\omega + i\Gamma + 2J_{\text{eff}} \sin k} \\
&= i^{d_{ll'}} \Omega^2 z_{\max}^{d_{ll'}/2} \int \frac{dk}{2\pi} \frac{e^{ik|d_{ll'}|}}{\omega + i\Gamma + 2J_{\text{eff}} \cos k}
\end{aligned}$$

for $2J > \Gamma$ and

$$\begin{aligned}
& \Sigma_{f, ll'}(\omega) \\
&= \Omega^2 \int_{|z|=\sqrt{z_{\max}}} \frac{dz}{2\pi iz} \frac{z^{d_{ll'}}}{\omega + i\Gamma + i(\frac{\Gamma}{2} - J)z + i(\frac{\Gamma}{2} + J)z^{-1}} \\
&= \Omega^2 z_{\max}^{d_{ll'}/2} \int_{|z|=1} \frac{dz}{2\pi iz} \frac{z^{d_{ll'}}}{\omega + i\Gamma + iJ_{\text{eff}}z + iJ_{\text{eff}}z^{-1}} \\
&= \Omega^2 z_{\max}^{d_{ll'}/2} \int \frac{dk}{2\pi} \frac{e^{ik|d_{ll'}|}}{\omega + i\Gamma + 2iJ_{\text{eff}} \cos k}
\end{aligned}$$

for $2J < \Gamma$. In the matrix form, the self-energy reads

$$\begin{aligned}
\Sigma_f(\omega) &= \Omega^2 \int \frac{dk}{2\pi} \frac{1}{\omega + i\Gamma + 2J_{\text{eff}} \cos k} + \Omega^2 \int \frac{dk}{2\pi} \\
&\quad \times \frac{e^{ikd}}{\omega + i\Gamma + 2J_{\text{eff}} \cos k} \begin{pmatrix} 0 & i^{-d} z_{\max}^{-d/2} \\ i^d z_{\max}^{d/2} & 0 \end{pmatrix}
\end{aligned}$$

for $2J > \Gamma$ and

$$\begin{aligned}
\Sigma_f(\omega) &= \Omega^2 \int \frac{dk}{2\pi} \frac{1}{\omega + i\Gamma + 2iJ_{\text{eff}} \cos k} + \Omega^2 \int \frac{dk}{2\pi} \\
&\quad \times \frac{e^{ikd}}{\omega + i\Gamma + 2iJ_{\text{eff}} \cos k} \begin{pmatrix} 0 & z_{\max}^{-d/2} \\ z_{\max}^{d/2} & 0 \end{pmatrix}
\end{aligned}$$

for $2J < \Gamma$, where d is the distance between two emitters.

By comparing the self-energies Σ_f and Σ , we can write the effective Hamiltonians

$$\begin{aligned}
\bar{H}_{\text{eff}} &= \Delta \sum_l a_l^\dagger a_l + \sum_k (-2J_{\text{eff}} \cos k - i\Gamma) b_k^\dagger b_k \\
&\quad + \frac{\Omega}{\sqrt{N}} \sum_k [(a_1^\dagger + i^d z_{\max}^{d/2} e^{ikd} a_2^\dagger) b_k \\
&\quad + b_k^\dagger (a_1 + i^{-d} z_{\max}^{-d/2} e^{-ikd} a_2)]
\end{aligned}$$

for $2J > \Gamma$ and

$$\begin{aligned}
\bar{H}_{\text{eff}} &= \Delta \sum_l a_l^\dagger a_l + \sum_k (-2iJ_{\text{eff}} \cos k - i\Gamma) b_k^\dagger b_k \\
&\quad + \frac{\Omega}{\sqrt{N}} \sum_k [(a_1^\dagger + z_{\max}^{d/2} e^{ikd} a_2^\dagger) b_k \\
&\quad + b_k^\dagger (a_1 + z_{\max}^{-d/2} e^{-ikd} a_2)]
\end{aligned}$$

for $2J < \Gamma$.

The analytic continuation and effective models allow us to diagonalize the Green function analytically as follows. For $2J > \Gamma$, the Green function

$$\begin{aligned}
G_f(\omega) &= \frac{1}{\omega - \Delta - \Sigma_f(\omega)} \\
&= S \begin{pmatrix} G_+(\omega) & 0 \\ 0 & G_-(\omega) \end{pmatrix} S^{-1} \quad (\text{A6})
\end{aligned}$$

is diagonalized in the “ \pm ” channels with eigenvalues

$$G_{\pm}(\omega) = \frac{1}{\omega - \Delta - \Sigma_{\pm}(\omega)}, \quad (\text{A7})$$

where the transformation

$$S = \frac{1}{\sqrt{2}} \begin{pmatrix} i^{-d/2} z_{\max}^{-d/4} & i^{-d/2} z_{\max}^{-d/4} \\ i^{d/2} z_{\max}^{d/4} & -i^{d/2} z_{\max}^{d/4} \end{pmatrix}$$

and the self-energy in the “ \pm ” channels can be obtained as

$$\begin{aligned}
\Sigma_{\pm}(\omega) &= \Omega^2 \int \frac{dk}{2\pi} \frac{1 \pm e^{ikd}}{\omega + i\Gamma + 2J_{\text{eff}} \cos k} \\
&= \begin{cases} -\frac{\Omega^2 [1 \pm z_{\pm}^d(\omega)]}{\sqrt{(\omega + i\Gamma)^2 - 4J_{\text{eff}}^2}}, & |z_{\pm}(\omega)| < 1, \\ \frac{\Omega^2 [1 \pm z_{\pm}^d(\omega)]}{\sqrt{(\omega + i\Gamma)^2 - 4J_{\text{eff}}^2}}, & |z_{\pm}(\omega)| < 1, \end{cases} \\
z_{\pm}(\omega) &= -\frac{\omega + i\Gamma}{2J_{\text{eff}}} \pm \sqrt{\frac{(\omega + i\Gamma)^2}{4J_{\text{eff}}^2} - 1}.
\end{aligned}$$

For $2J < \Gamma$, the Green functions have the same forms as Eqs. (A6) and (A7), where

$$S = \frac{1}{\sqrt{2}} \begin{pmatrix} z_{\max}^{-d/4} & z_{\max}^{-d/4} \\ z_{\max}^{d/4} & -z_{\max}^{d/4} \end{pmatrix}$$

and the self-energy is

$$\begin{aligned}
\Sigma_{\pm}(\omega) &= \Omega^2 \int \frac{dk}{2\pi} \frac{1 \pm e^{ikd}}{\omega + i\Gamma + 2iJ_{\text{eff}} \cos k} \\
&= \begin{cases} i \frac{\Omega^2 [1 \pm z_{\pm}^d(\omega)]}{\sqrt{-(\omega + i\Gamma)^2 - 4J_{\text{eff}}^2}}, & |z_{\pm}(\omega)| < 1, \\ -i \frac{\Omega^2 [1 \pm z_{\pm}^d(\omega)]}{\sqrt{-(\omega + i\Gamma)^2 - 4J_{\text{eff}}^2}}, & |z_{\pm}(\omega)| < 1, \end{cases} \\
z_{\pm}(\omega) &= i \frac{\omega + i\Gamma}{2J_{\text{eff}}} \pm \sqrt{-\frac{(\omega + i\Gamma)^2}{4J_{\text{eff}}^2} - 1}.
\end{aligned}$$

Eventually, the dynamics of emitters is completely determined by the analytic structure of $G_{\pm}(\omega)$ that is obtained analytically.

For $2J > \Gamma$, the Fourier transform of the Green functions

$$\begin{aligned} G_{\sigma}(\omega) &= \sum_s \frac{Z_s^{\sigma}}{\omega - \varepsilon_s^{\sigma}} + \int_{-2J_{\text{eff}}}^{2J_{\text{eff}}} \frac{dx}{2\pi i} \frac{\sqrt{4J_{\text{eff}}^2 - x^2}}{\omega - x + i\Gamma} \\ &\times \left\{ \frac{1}{\sqrt{4J_{\text{eff}}^2 - x^2}(x - i\Gamma - \Delta) - i\Omega^2[1 + \sigma z_-^d(x - i\Gamma)]}} \right. \\ &\left. - \frac{1}{\sqrt{4J_{\text{eff}}^2 - x^2}(x - i\Gamma - \Delta) + i\Omega^2[1 + \sigma z_+^d(x - i\Gamma)]}} \right\} \end{aligned}$$

in the $\sigma = \pm$ channels results in

$$\begin{aligned} G_{\sigma}(t) &= -i \sum_s Z_s^{\sigma} e^{-i\varepsilon_s^{\sigma} t} - \int_{-2J_{\text{eff}}}^{2J_{\text{eff}}} \frac{dx}{2\pi} e^{-i(x-i\Gamma)t} \sqrt{4J_{\text{eff}}^2 - x^2} \\ &\times \left\{ \frac{1}{\sqrt{4J_{\text{eff}}^2 - x^2}(x - i\Gamma - \Delta) - i\Omega^2[1 + \sigma z_-^d(x - i\Gamma)]}} \right. \\ &\left. - \frac{1}{\sqrt{4J_{\text{eff}}^2 - x^2}(x - i\Gamma - \Delta) + i\Omega^2[1 + \sigma z_+^d(x - i\Gamma)]}} \right\}, \end{aligned}$$

where ε_s^{σ} and Z_s^{σ} are the poles and the corresponding residues

$$Z_s^{\sigma} = \frac{1}{1 - \partial_{\omega} \Sigma_{\sigma}(\omega)|_{\omega=\varepsilon_s^{\sigma}}}$$

of G_{σ} .

For $2J < \Gamma$, the Fourier transform of the Green functions

$$\begin{aligned} G_{\sigma}(\omega) &= \sum_s \frac{Z_s^{\sigma}}{\omega - \varepsilon_s^{\sigma}} - \int_{-2J_{\text{eff}}}^{2J_{\text{eff}}} \frac{dx}{2\pi} \frac{\sqrt{4J_{\text{eff}}^2 - x^2}}{\omega - ix + i\Gamma} \\ &\times \left\{ \frac{1}{\sqrt{4J_{\text{eff}}^2 - x^2}(x - \Gamma + i\Delta) + i\Omega^2[1 + \sigma z_-^d(ix - i\Gamma)]}} \right. \\ &\left. - \frac{1}{\sqrt{4J_{\text{eff}}^2 - x^2}(x - \Gamma + i\Delta) - i\Omega^2[1 + \sigma z_+^d(ix - i\Gamma)]}} \right\} \end{aligned}$$

leads to

$$\begin{aligned} G_{\sigma}(t) &= -i \sum_s Z_s^{\sigma} e^{-i\varepsilon_s^{\sigma} t} + \int_{-2J_{\text{eff}}}^{2J_{\text{eff}}} \frac{dx}{2\pi} e^{-(\Gamma-x)t} \sqrt{4J_{\text{eff}}^2 - x^2} \\ &\times \left\{ \frac{1}{\sqrt{4J_{\text{eff}}^2 - x^2}(x - \Gamma + i\Delta) - i\Omega^2[1 + \sigma z_+^d(ix - i\Gamma)]}} \right. \\ &\left. - \frac{1}{\sqrt{4J_{\text{eff}}^2 - x^2}(x - \Gamma + i\Delta) + i\Omega^2[1 + \sigma z_-^d(ix - i\Gamma)]}} \right\}. \end{aligned}$$

3. Two excitations

In the two-excitation subspace of a single emitter, the dynamics is determined by the retarded Green function

$$\begin{aligned} D(t) &= -i \frac{1}{2} \langle [a^2(t), a^{\dagger 2}(0)] \rangle \theta(t) \\ &= -i \frac{1}{2} \langle a^2(t) a^{\dagger 2}(0) \rangle \theta(t), \end{aligned}$$

where the second equation is valid for the initial vacuum state. As shown in Fig. 11, the Fourier transform $D^R(\omega) = \int dt e^{i\omega t} D(t)$ of $D(t)$ can be obtained by the Dyson expansion of the on-site interaction U as

$$D^R(\omega) = \frac{1}{\Pi^{-1}(\omega) - U},$$

where

$$\Pi(\omega) = i \int \frac{d\omega'}{2\pi} G^K(\omega') G^R(\omega - \omega')$$

is the convolution of G^K and G^R . For the general nonequilibrium problem, G^K , G^R , and G^A are three independent Green functions, and the fluctuation-dissipation theorem $G^K(\omega) = [1 \pm 2n(\omega)][G^R(\omega) - G^A(\omega)]$ is satisfied only in the equilibrium state. In the present case, the nature of the bath in zero temperature results in the relation $G^K(\omega) = G^R(\omega) - G^A(\omega)$ that can also be checked directly from Eq. (A1). As a result, the convolution becomes

$$\begin{aligned} \Pi(\omega) &= i \int \frac{d\omega'}{2\pi} [G^R(\omega') - G^A(\omega')] G^R(\omega - \omega') \\ &= i \int \frac{d\omega'}{2\pi} G^R(\omega') G^R(\omega - \omega'), \end{aligned} \quad (\text{A8})$$

where in the second equation the causality condition is used.

To perform the Fourier transform $D(t) = \int (d\omega/2\pi) D^R(\omega) e^{-i\omega t}$ efficiently, we introduce the analytic continuation

$$D_f(\omega) = \frac{1}{\Pi_f^{-1}(\omega) - U} \quad (\text{A9})$$

of $D^R(\omega)$, where

$$\Pi_f(\omega) = i \int \frac{d\omega'}{2\pi} G_f(\omega') G_f(\omega - \omega').$$

Since in the integral contour of the Fourier transform $D^R(\omega) = D_f(\omega)$, the Fourier transform $D(t) = \int (d\omega/2\pi) D_f(\omega) e^{-i\omega t}$. Compared with the original convolution (A8), $\Pi_f(\omega)$ has the simple structure of G_f , i.e., as shown in the first subsection the simple behaviors in the vicinity of poles and branch cuts, we can calculate $\Pi_f(\omega)$ and $D^R(\omega)$ as well as the Fourier transform efficiently.

Appendix B: Steady-state correlation functions of the driven emitter

1. Master equation without driving

Our starting point is the master equation (5) without the drive ($\epsilon = 0$), i.e.,

$$\begin{aligned}\dot{\rho} &= \mathcal{L}_0\rho \\ &= -i[H_0, \rho] - \frac{\Gamma}{2} \sum_j \left(\{O_j^\dagger O_j, \rho\} + 2O_j\rho O_j^\dagger \right).\end{aligned}\quad (\text{B1})$$

Here, $H_0 = H_{\text{emit}} + H_{\text{sb}} + H_b$, where the Hamiltonian for an undriven emitter is $H_{\text{emit}} = \Delta a^\dagger a + (U/2)a^\dagger a^\dagger a a$, the emitter-bath coupling $H_{\text{sb}} = \Omega a^\dagger b_0 + \text{H.c.}$, and $H_b = \sum_j J e^{i\theta} b_j^\dagger b_{j+1} + \text{H.c.}$ The jump operator in Eq. (B1) is $O_j = b_j + b_{j+1}$. We stress that the effective Hamiltonian

$$H_{\text{eff}} = H_0 - i\frac{\Gamma}{2} \sum_j O_j^\dagger O_j \quad (\text{B2})$$

commutes with the total particle number $N = a^\dagger a + \sum_j b_j^\dagger b_j$:

$$[H_{\text{eff}}, N] = 0. \quad (\text{B3})$$

In this section, we present the approach to systematically calculate the quantum correlation functions of the weakly driven emitter in the steady state of the master equation (5). First, in Appendix B 1, we consider an undriven emitter and show that the spontaneous emission of n excitations is fully determined by the retarded n -particle Green function (of the emitter) in the vacuum state. Then, in Appendix B 2, we take into account the weak driving field in the master equation. Following Refs. [63, 64], we develop a perturbative solution and connect the physical observables of the driven emitter with Green functions of the undriven case.

Thus, the number of excitations is preserved in the nonunitary time evolution driven by H_{eff} . Consequently, the steady state of Eq. (B1) at zero temperature is the vacuum state $|0\rangle$.

We now show that the dynamics for the initial pure state $\rho(0) = |\psi(0)\rangle \langle \psi(0)|$ with finite n excitations can be efficiently studied using H_{eff} . Exploiting the property (B3), the Dyson expansion gives rise to the formal solution

$$\begin{aligned}\rho(t) &= e^{-iH_{\text{eff}}t} \rho(0) e^{iH_{\text{eff}}^\dagger t} + \Gamma \sum_{j_1} \int_0^t ds_1 e^{-iH_{\text{eff}}(t-s_1)} O_{j_1} e^{-iH_{\text{eff}}s_1} \rho(0) e^{iH_{\text{eff}}^\dagger s_1} O_{j_1}^\dagger e^{iH_{\text{eff}}^\dagger(t-s_1)} \\ &\quad + \Gamma^2 \sum_{j_1, j_2} \int_0^t ds_1 \int_0^{s_1} ds_2 e^{-iH_{\text{eff}}(t-s_1)} O_{j_1} e^{-iH_{\text{eff}}(s_1-s_2)} O_{j_2} e^{-iH_{\text{eff}}s_2} \rho(0) e^{iH_{\text{eff}}^\dagger s_2} O_{j_2}^\dagger e^{iH_{\text{eff}}^\dagger(s_1-s_2)} O_{j_1}^\dagger e^{iH_{\text{eff}}^\dagger(t-s_1)} + \dots \\ &= \left| \psi^{(0)}(t) \right\rangle \left\langle \psi^{(0)}(t) \right| + \Gamma \sum_{j_1} \int_0^t ds_1 \left| \psi_{j_1}^{(1)}(t, s_1) \right\rangle \left\langle \psi_{j_1}^{(1)}(t, s_1) \right| \\ &\quad + \Gamma^2 \sum_{j_1, j_2} \int_0^t ds_1 \int_0^{s_1} ds_2 \left| \psi_{j_1, j_2}^{(2)}(t, s_1, s_2) \right\rangle \left\langle \psi_{j_1, j_2}^{(2)}(t, s_1, s_2) \right| + \dots\end{aligned}\quad (\text{B4})$$

Here the density matrix $\rho(t)$ is an incoherent superposi-

tion of states $|\psi^{(0)}(t)\rangle$, $|\psi_{j_1}^{(1)}(t, s_1)\rangle$, etc., where each of them is governed by the effective Hamiltonian H_{eff} in the corresponding subspace, i.e.,

$$\begin{aligned}
|\psi^{(0)}(t)\rangle &= e^{-iH_{\text{eff}}t} |\psi(0)\rangle, \\
|\psi_{j_1}^{(1)}(t, s_1)\rangle &= e^{-iH_{\text{eff}}(t-s_1)} O_{j_1} e^{-iH_{\text{eff}}s_1} |\psi(0)\rangle, \\
|\psi_{j_1, j_2}^{(2)}(t, s_1, s_2)\rangle &= e^{-iH_{\text{eff}}(t-s_1)} O_{j_1} e^{-iH_{\text{eff}}(s_1-s_2)} O_{j_2} e^{-iH_{\text{eff}}s_2} |\psi(0)\rangle.
\end{aligned} \tag{B5}$$

Since the jump operator always depletes excitations from the system, the series in Eq. (B4) is automatically truncated after acting the jump operator $n + 1$ times. As a result, we have to study only the dynamics of the initial pure state $|\psi(0)\rangle$ governed by the effective Hamiltonian H_{eff} , where the transition between the subspaces with different excitation numbers is described by the jump operator.

It follows from Eqs. (B4) and (B5) that the spontaneous emission probability of n excitations in the undriven emitter is given by

$$P_n = \text{tr}[|n\rangle \langle n| \rho(t)] = |\langle n| e^{-iH_{\text{eff}}t} |n\rangle|^2. \tag{B6}$$

This is just the norm square of the n -particle Green function G_n^R in the vacuum state, which is completely determined by H_{eff} .

In summary, we can solve the full dynamics of the emitter first in subspaces with different excitation numbers governed by the effective Hamiltonian H_{eff} and then connect the results using the jump operator. Interestingly, for the trivial steady state $|0\rangle$, since $H_{\text{eff}}|0\rangle = 0$, the dynamics in the subspace with n excitations is described by

$$\begin{aligned}
G_n^R(\omega) &= -i \frac{1}{n!} \int dt e^{i\omega t} \langle 0| [a^n(t), a^{\dagger n}(0)] |0\rangle \theta(t) \\
&= -i \frac{1}{n!} \int_0^\infty dt e^{i\omega t} \langle 0| a^n(t) a^{\dagger n}(0) |0\rangle \theta(t).
\end{aligned} \tag{B7}$$

Thus, the fluctuation-dissipation theorem holds in the subspace for Green functions of the emitter in the vacuum state, even though the system state is out of equilibrium.

2. Weakly driven system

With the above results, we now consider the case when the emitter is driven by an external field with the driving frequency ω_d and the driving strength $\epsilon \neq 0$. In the rotating framework with respect to ω_d , the master equation reads

$$\dot{\rho} = \mathcal{L}_0 \rho + \mathcal{L}_\epsilon(t) \rho \tag{B8}$$

where \mathcal{L}_0 is the Liouvillian for the undriven system and \mathcal{L}_ϵ describes the driving field with the strength ϵ :

$$\mathcal{L}_\epsilon(t) \rho = -i[\epsilon(A^\dagger + A), \rho], \tag{B9}$$

with the operator $A = ae^{i\omega_d t}$ in our case.

In general, one has to solve the master equation (B8) numerically to study the full dynamics. However, there are also special cases which allow us to obtain the steady state and time evolution analytically. It turns out that, for the weak driving strength ϵ much smaller than the spectral gap of the Liouvillian \mathcal{L} without the driving term and the steady state of \mathcal{L} is not degenerate, the dynamics can also be studied using the Green functions G_n^R in subspaces with different excitations. This statement has been proven in Ref. [63] and applied to study photon pair generation in Ref. [48]. In the following, we use it for our case.

Specifically, we can expand $\rho(t)$ to some order of ϵ for corresponding problems. For our purpose of calculating the second-order correlation function, we expand $\rho(t)$ up to the fourth order of ϵ (the n th-order term is denoted by ρ_n , $n = 0, 1, \dots, 4$). For the vacuum steady state $\rho_0 = |0\rangle \langle 0|$ of the undriven system, we obtain

$$\begin{aligned}
\rho(t) &= \mathcal{T} e^{\int_0^t [\mathcal{L}_0 + \mathcal{L}_\epsilon(t_1)] dt_1} \rho_0 \\
&= \rho_0 + \rho_1(t) + \rho_2(t) + \rho_3(t) + \rho_4(t) \\
&= e^{\mathcal{L}_0 t} \rho_0 + \int_0^t ds_1 e^{\mathcal{L}_0(t-s_1)} \mathcal{L}_\epsilon e^{\mathcal{L}_0 s_1} \rho_0 + \int_0^t ds_1 \int_0^{s_1} ds_2 e^{\mathcal{L}_0(t-s_1)} \mathcal{L}_\epsilon e^{\mathcal{L}_0(s_1-s_2)} \mathcal{L}_\epsilon e^{\mathcal{L}_0 s_2} \rho_0 \\
&\quad + \int_0^t ds_1 \int_0^{s_1} ds_2 \int_0^{s_2} ds_3 e^{\mathcal{L}_0(t-s_1)} \mathcal{L}_\epsilon e^{\mathcal{L}_0(s_1-s_2)} \mathcal{L}_\epsilon e^{\mathcal{L}_0(s_2-s_3)} \mathcal{L}_\epsilon e^{\mathcal{L}_0 s_3} \rho_0 \\
&\quad + \int_0^t ds_1 \int_0^{s_1} ds_2 \int_0^{s_2} ds_3 \int_0^{s_3} ds_4 e^{\mathcal{L}_0(t-s_1)} \mathcal{L}_\epsilon e^{\mathcal{L}_0(s_1-s_2)} \mathcal{L}_\epsilon e^{\mathcal{L}_0(s_2-s_3)} \mathcal{L}_\epsilon e^{\mathcal{L}_0(s_3-s_4)} \mathcal{L}_\epsilon e^{\mathcal{L}_0 s_4} \rho_0.
\end{aligned} \tag{B10}$$

By using Eq. (B4), and keeping in mind that the

undriven effective Hamiltonian H_{eff} [see Eq. (B2)] is

number conserving, we calculate Eq. (B10) as

$$\begin{aligned}
\rho(t) = & \rho_0 - i\varepsilon \int_0^t ds_1 \left[e^{-iH_{\text{eff}}(t-s_1)} A^\dagger \rho_0 - \rho_0 A e^{iH_{\text{eff}}^\dagger(t-s_1)} \right] \\
& - \varepsilon^2 \int_0^t ds_1 \int_0^{s_1} ds_2 \left[e^{-iH_{\text{eff}}(t-s_1)} A^\dagger e^{-iH_{\text{eff}}(s_1-s_2)} A^\dagger \rho_0 + \rho_0 A e^{iH_{\text{eff}}^\dagger(s_1-s_2)} A e^{iH_{\text{eff}}^\dagger(t-s_1)} \right] \\
& + \varepsilon^2 \Gamma \sum_{j_1} \int_0^t ds_1 \int_0^{s_1} ds_2 \int_0^{t-s_1} ds_3 e^{-iH_{\text{eff}}(t-s_1-s_3)} O_{j_1} e^{-iH_{\text{eff}} s_3} \left[e^{-iH_{\text{eff}}(s_1-s_2)} A^\dagger \rho_0 A \right. \\
& \left. + A^\dagger \rho_0 A e^{iH_{\text{eff}}^\dagger(s_1-s_2)} \right] e^{iH_{\text{eff}}^\dagger s_3} O_{j_1}^\dagger e^{iH_{\text{eff}}^\dagger(t-s_1-s_3)} \\
& + \varepsilon^2 \int_0^t ds_1 \int_0^{s_1} ds_2 \left[e^{-iH_{\text{eff}}(t-s_2)} A^\dagger \rho_0 A e^{iH_{\text{eff}}^\dagger(t-s_1)} + e^{-iH_{\text{eff}}(t-s_1)} A^\dagger \rho_0 A e^{iH_{\text{eff}}^\dagger(t-s_2)} \right] \\
& - \varepsilon^2 \int_0^t ds_1 \int_0^{s_1} ds_2 \left[\rho_0 A e^{iH_{\text{eff}}^\dagger(s_1-s_2)} A^\dagger + A e^{-iH_{\text{eff}}(s_1-s_2)} A^\dagger \rho_0 \right] + \rho_3(t) + \rho_4(t), \tag{B11}
\end{aligned}$$

where the third-order and fourth-order terms are useful for the excitation statistics. Finally, the steady state ρ_{ss} is obtained as taking $t \rightarrow \infty$.

Note that one can benchmark the above derivations using a two-level system with $A = \sigma^-$, $H_0 = 0$, and the jump operator σ^- . In this case, following similar steps, the steady-state density matrix up to ε^2 is derived as

$$\rho_{\text{ss}} \sim \left(1 - \frac{4\varepsilon^2}{\gamma^2}\right) |g\rangle \langle g| - i \frac{2\varepsilon}{\gamma} (|e\rangle \langle g| - |g\rangle \langle e|) + \frac{4\varepsilon^2}{\gamma^2} |e\rangle \langle e|,$$

which is exactly the steady-state solution

$$\rho_{\text{ss}} = \frac{4\varepsilon^2 + \gamma^2}{8\varepsilon^2 + \gamma^2} |g\rangle \langle g| - \frac{2i\varepsilon\gamma}{8\varepsilon^2 + \gamma^2} (|e\rangle \langle g| - |g\rangle \langle e|) + \frac{4\varepsilon^2}{8\varepsilon^2 + \gamma^2} |e\rangle \langle e|$$

of the Liouvillian $\mathcal{L}_0 + \mathcal{L}_\varepsilon$ up to the order ε^2 .

Now we are ready to calculate for our case the first- and second-order correlation functions of the driven emitter in the steady state. Keeping the second-order terms in Eq. (B11), we obtain

$$\langle a^\dagger a \rangle_{\text{ss}} = \varepsilon^2 \left| \langle 0 | a \frac{1}{\omega_d - H_{\text{eff}}} a^\dagger | 0 \rangle \right|^2. \tag{B12}$$

Keeping the fourth-order terms in Eq. (B11), we obtain

$$\begin{aligned}
& \langle a^\dagger a^\dagger(\tau) a(\tau) a \rangle_{\text{ss}} \\
& = \text{Tr} \left[a e^{\mathcal{L}\tau} (a \rho_{\text{ss}} a^\dagger) a^\dagger \right] \\
& = \text{Tr} \left[a e^{\mathcal{L}_0 \tau} \int_0^\tau ds_1 \int_0^{s_1} ds_2 \mathcal{L}_\varepsilon(s_1) \mathcal{L}_\varepsilon(s_2) (a \rho_2 a^\dagger) a^\dagger \right] + \text{Tr} \left[a e^{\mathcal{L}_0 \tau} \int_0^\tau ds_1 \mathcal{L}_\varepsilon(s_1) (a \rho_3 a^\dagger) a^\dagger \right] + \text{Tr} \left[a e^{\mathcal{L}_0 \tau} (a \rho_4 a^\dagger) a^\dagger \right] \\
& = \varepsilon^4 \left| \langle 0 | a \frac{1 - e^{i(\omega_d - H_{\text{eff}})\tau}}{\omega_d - H_{\text{eff}}} a^\dagger | 0 \rangle \langle 0 | a \frac{1}{\omega_d - H_{\text{eff}}} a^\dagger | 0 \rangle + \langle 0 | a e^{i(\omega_d - H_{\text{eff}})\tau} a \frac{1}{2\omega_d - H_{\text{eff}}} a^\dagger \frac{1}{\omega_d - H_{\text{eff}}} a^\dagger | 0 \rangle \right|^2, \tag{B13}
\end{aligned}$$

where the quantum regression theorem is used in the second row.

The correlation functions (B12) and (B13) can be written in terms of Green functions on the vacuum state. In

the compact form, we have

$$\begin{aligned}
\frac{\langle a^\dagger a \rangle_{\text{ss}}}{\varepsilon^2} & = \left| \int_{-\infty}^{\infty} dt e^{-i\omega_d t} \langle 0 | \mathcal{T} a(0) a^\dagger(t) | 0 \rangle \right|^2 \\
\frac{\langle a^\dagger a^\dagger(\tau) a(\tau) a \rangle_{\text{ss}}}{\varepsilon^4} & = \left| \int_{-\infty}^{+\infty} dt_1 dt_2 e^{-i\omega_d(t_1+t_2)} G(\tau; t_1, t_2) \right|^2, \tag{B14}
\end{aligned}$$

with $G(\tau; t_1, t_2) = -i \langle 0 | \mathcal{T} a(\tau) a(0) a^\dagger(t_1) a^\dagger(t_2) | 0 \rangle / 2$,

where $a(t) = e^{iH_{\text{eff}}^\dagger t} a e^{-iH_{\text{eff}} t}$ is governed by the undriven effective Hamiltonian and the Green functions are all defined on the vacuum state.

From the above analysis, we show explicitly that, even though our system is weakly driven, the relevant physical

observables of the system can be calculated from Green functions of the undriven system in the vacuum state, which is governed by H_{eff} . In the explicit form, the normalized second-order correlation function is found as

$$g^{(2)}(\tau) = \frac{\left| \langle 0 | a \frac{1 - e^{i(\omega_d - H_{\text{eff}})\tau}}{\omega_d - H_{\text{eff}}} a^\dagger | 0 \rangle \langle 0 | a \frac{1}{\omega_d - H_{\text{eff}}} a^\dagger | 0 \rangle + \langle 0 | a e^{i(\omega_d - H_{\text{eff}})\tau} a \frac{1}{2\omega_d - H_{\text{eff}}} a^\dagger \frac{1}{\omega_d - H_{\text{eff}}} a^\dagger | 0 \rangle \right|^2}{\left| \langle 0 | a \frac{1}{\omega_d - H_{\text{eff}}} a^\dagger | 0 \rangle \right|^4}. \quad (\text{B15})$$

It is completely determined by the spectral properties of the effective Hamiltonian H_{eff} in the single- or two-excitation subspaces, respectively. Therefore, once the eigenproblem of H_{eff} in the undriven case is solved, we can obtain $g^{(2)}(\tau)$.

Based on Eq. (B14), we can now apply the Dyson expansion as illustrated in Fig. 11 to calculate the right side and obtain

$$g^{(2)}(\tau) = \left| 1 + \left[i \int \frac{d\omega'}{2\pi} G^R(\omega') G^R(-\omega') e^{-i\omega'\tau} \right] T(0) \right|^2. \quad (\text{B16})$$

Here, the poles and branch cuts of

$$T(\omega) = \frac{1}{U^{-1} - i \int \frac{d\omega'}{2\pi} G^R(\omega') G^R(\omega - \omega')}$$

correspond to the quasibound state and continuum of H_{eff} in the two-excitation subspace. This eventually leads to Eq. (2) in our text.

Appendix C: Scaling behaviors in quantum Zeno regimes

In this section, we study the scaling behaviors in the quantum Zeno regime. In parallel with Appendix A, we investigate the analytic structure of $G_f(\omega)$ and $G_\sigma(\omega)$ for the large Γ in Appendixes C1 and C2. The approximate analytical expressions of Green functions $G^R(\omega)$ in the time domain are achieved, which agree with the exact results quantitatively. In Appendix C3, the effective Hamiltonian for two excitations is derived via the perturbation theory, which gives rise to the scaling behavior in a good agreement with the exact solution.

1. Single emitter

In the large Γ limit, the leading order in the Taylor expansion of $G_f^{-1}(\omega)$ leads to two poles $\epsilon_{s=\pm} = i(\Omega^4/2)^{1/3} e^{i(2\pi s/3)} \Gamma^{-1/3}$ for the resonant case $\Delta = 0$ and

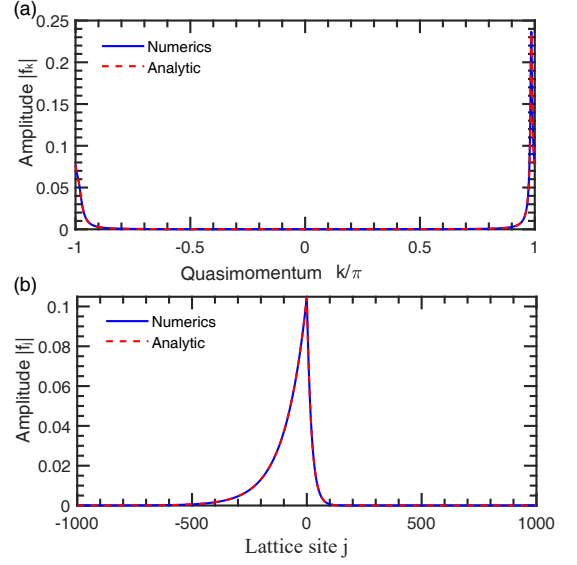


Figure 12. Comparison between the analytic and numerical results for the bath component of the single-emitter quasi-bound state in (a) momentum space and (b) real space representation. In both (a) and (b), the numerical results (blue solid curves) are obtained from diagonalizing the effective Hamiltonian H_{eff} with the open-bath size $N_b = 2000$, the emitter detuning $\Delta = 0$, bath dissipation strength $\Gamma/J = 100$, and the coupling strength $\Omega/J = 1$. The analytical results (red dashed curves) in (a) are obtained from Eq. (C2) and in (b) are obtained from Eq. (C3).

two poles

$$\begin{aligned} \Sigma_f(\omega) &= \frac{i\Omega^2 \text{sgn}[1 - |z_-(\omega)|]}{\sqrt{-(\omega + i\Gamma)^2 - 4J_{\text{eff}}^2}}, \\ z_-(\omega) &= i \frac{\omega + i\Gamma}{2J_{\text{eff}}} - \sqrt{-\frac{(\omega + i\Gamma)^2}{4J_{\text{eff}}^2} - 1} \\ \omega &= i \left(\frac{\Omega^4}{2\Gamma} \right)^{1/3} e^{i(2\pi/3)s} \\ \text{sgn}[1 - |z_-(\omega)|] &= -1 \end{aligned}$$

$$\begin{aligned}\varepsilon_1 &= \Delta - i \frac{\Omega^2}{\sqrt{2\Delta}} e^{i(\pi/4)} \Gamma^{-1/2}, \\ \varepsilon_2 &= -i \left(\frac{\Omega^4}{2\Delta^2} + 2J^2 \right) \frac{1}{\Gamma}\end{aligned}$$

for the finite Δ .

We can also analytically obtain the wave function of the quasibound states with the complex energy ε_s . Without loss of generality, here we focus on the case $\Delta = 0$. In the momentum space representation, the quasibound state is $|B\rangle = c_1 a_1^\dagger |0\rangle + \sum_k f_k b_k^\dagger |0\rangle$, where c_1 and f_k are coefficients. The c_1 can be obtained via the residue Z_s of the Green function at $\omega = \varepsilon_s$ [see Eq. (A3)], giving

$$c_1 = Z_s = \frac{\varepsilon_s^2 + 2i\Gamma\varepsilon_s - 4J^2}{2\varepsilon_s^2 + 3i\Gamma\varepsilon_s - 4J^2}. \quad (\text{C1})$$

In the limit $\Gamma/(2J) \rightarrow \infty$, $c_1 \rightarrow 2/3$. The f_k can be calculated using the self-energy matrix element in Eq. (A5) with $\omega = \varepsilon_s$, giving

$$f_k = \frac{\Omega c_1}{\sqrt{N_b}} \frac{1}{\varepsilon_s - (\varepsilon_k - i\gamma_k)}, \quad (\text{C2})$$

where in our case $\varepsilon_k = 2J \sin(k)$ and $\gamma_k = \Gamma[1 + \cos(k)]$. In Fig. 12(a), we show the numerical result (solid curve) of $|f_k|$ by diagonalizing the effective Hamiltonian H_{eff} and compare it with Eq. (C2). A good agreement is found.

In real space, the quasibound state is $|B\rangle = c_1 a_1^\dagger |0\rangle + \sum_j f_j b_j^\dagger |0\rangle$, where f_j is the amplitude of the bath component at lattice site j . Noting that the emitter is locally coupled to b_0 , the f_j can be obtained from the self-energy matrix element (A5) with $\omega = \varepsilon_s$, which yields

$$f_j = \frac{\Sigma_{j0}(\varepsilon_s)}{\Omega} c_1, \quad (\text{C3})$$

where for $\Gamma/(2J) > 1$ we have

$$\begin{aligned}\Sigma_{j0}(\omega) &= \begin{cases} -i \frac{\Omega^2 e^{j \ln \beta_+}}{\sqrt{-(\omega+i\Gamma)^2 - 4J_{\text{eff}}^2}}, & (j > 0) \\ -i \frac{\Omega^2 e^{-j \ln \beta_-}}{\sqrt{-(\omega+i\Gamma)^2 - 4J_{\text{eff}}^2}}, & (j < 0) \end{cases} \\ \beta_{\pm}(\omega) &= \frac{i(\omega + i\Gamma) + \sqrt{-(\omega + i\Gamma)^2 - 4J_{\text{eff}}^2}}{\Gamma \pm 2J} \end{aligned} \quad (\text{C4})$$

with $J_{\text{eff}} = \sqrt{\Gamma^2/4 - J^2}$. In Fig. 12(b), we numerically calculate $|f_j|$ by diagonalizing H_{eff} in real space. We see that the numerical results (solid curve) agree very well with that obtained from Eq. (C3). Note that, in general, $\beta_+ \neq \beta_-$, and, therefore, the quasibound state has a different localization length on the left and right sides of the emitter.

In the limit $\Gamma/(2J) \rightarrow \infty$, where $\beta_+ \approx \beta_-$, one can obtain a simplified expression for the average momentum k_b and the average localization length l_b of the bath component. In this limit, we find $\ln \beta_{\pm} \approx i\pi - \sqrt{-2i\varepsilon_s/\Gamma}$. Using, e.g., $\varepsilon_s = \frac{1}{2}(\sqrt{3} - i)(\Omega^4/2)^{1/3} \Gamma^{-1/3}$, we obtain

$e^{j \ln \beta_+} = e^{-ij k_b - j/l_b}$, where

$$k_b = \pi - \frac{\sqrt{3}}{2^{2/3}} \left(\frac{\Omega}{\Gamma} \right)^{2/3}, \quad (\text{C5})$$

$$l_b = 2^{2/3} \left(\frac{\Gamma}{\Omega} \right)^{2/3}. \quad (\text{C6})$$

Thus, when $\Gamma/(2J) \rightarrow \infty$, $k_b \rightarrow \pi$, and l_b increases as $(\Gamma/\Omega)^{2/3}$. In Fig. 12(a), the momentum at which the peak occurs is well described by Eq. (C5).

2. Two emitters

For two emitters, we solve the equations $1/G_{\pm}(\varepsilon) = 0$ to obtain the poles for the resonant case $\Delta = 0$. Here, we focus on only the even distance d , since for the odd distance it turns out that the physics is the same by interchanging the $+$ and $-$ channels. In the even channel, the leading term in the Taylor expansion of $1/G_+(\varepsilon)$ results in the same scaling behavior $\varepsilon_{s=\pm} = i(2\Omega^4)^{1/3} e^{i(2\pi s/3)} \Gamma^{-1/3}$ with the prefactor enhanced by a factor of $4^{1/3}$. In the odd channel, two poles are

$$\varepsilon_s = sR - i \frac{\Omega^2 d}{\Gamma},$$

where the positive $R \sim \Gamma^{-2}$ for $\Omega > \sqrt{2/d}J$. For the small $\Omega < \sqrt{2/d}J$, two poles merge into a single pole $\varepsilon = -i\Omega^2 d/\Gamma$.

In the $+$ channel, the residues $Z_s \sim 2/3$ and the contribution from the branch cut is negligible, which leads to

$$G_+(t) \sim -i \frac{4}{3} e^{-(\Omega^4/4\Gamma)^{1/3} t} \cos \left[\sqrt{3} \left(\frac{\Omega^4}{4\Gamma} \right)^{1/3} t \right].$$

In the $-$ channel, the residues $Z_s \sim 1$ and the contribution from the branch cut cancels that from one residue for $\Omega > \sqrt{2/d}J$. For the small $\Omega < \sqrt{2/d}J$, the contribution from the branch cut is negligible, and only a single pole with residue $Z_s \sim 1$ survives. As a result, the Green function reads

$$G_-(t) \sim -i e^{-(\Omega^2 d/\Gamma)t}.$$

The transformation S leads to

$$\begin{aligned}iG_{11}^R(t) &= \frac{2}{3} e^{-(\Omega^4/4\Gamma)^{1/3} t} \cos \left[\sqrt{3} \left(\frac{\Omega^4}{4\Gamma} \right)^{1/3} t \right] + \frac{1}{2} e^{-(\Omega^2 d/\Gamma)t}, \\ iG_{12}^R(t) &= \frac{2}{3} e^{-(\Omega^4/4\Gamma)^{1/3} t} \cos \left[\sqrt{3} \left(\frac{\Omega^4}{4\Gamma} \right)^{1/3} t \right] - \frac{1}{2} e^{-(\Omega^2 d/\Gamma)t}.\end{aligned}$$

3. Effective models of two excitations

In this subsection, we derive the effective Hamiltonian in the two-excitation subspace using the perturbation theory, where Δ is finite and the resonance condition $U = -\Delta$ is assumed. The two-excitation sector

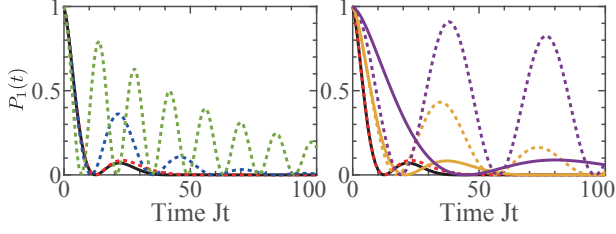


Figure 13. Spontaneous emission of single excitation in an emitter coupled to a strongly open bath with the finite size N_b . The solid curves denote the result obtained via the Green function approach, and the dashed line denotes the results obtained using the corresponding non-Hermitian Hamiltonian with a finite N_b , detuning $\Delta/J = 0$ and Rabi frequency $\Omega/J = 1$. (a) Results for $N_b = 20, 60, 150$ (green, blue, and red line, respectively) and the bath dissipation rate $\Gamma/2J = 100$. The corresponding α in Eq. (E1) is $\alpha = 0.1, 0.9, 5.7$. (b) Results for $\Gamma/2J = 100, 500, 5000$ (red, yellow, and purple line, respectively) and $N_b = 150$, corresponding to $\alpha = 5.7, 1.1, 0.1$.

is spanned in the basis $\{a^{\dagger 2}|0\rangle/\sqrt{2} \equiv |d\rangle, a^\dagger b_k^\dagger|0\rangle \equiv |k\rangle_e, b_k^\dagger b_{k'}^\dagger|0\rangle \equiv |kk'\rangle\}$. Under the condition $U = -\Delta$, the doublon state $|d\rangle$ and states $|k\rangle_e$ are nearly degenerate. We can adiabatically eliminate the states $|kk'\rangle$ as

$$H_2'' = H_0 + \sum_k \frac{\Omega^2}{N} \sum_p \frac{1}{\Delta - \bar{\omega}_p} |k\rangle_e \langle k| + \frac{\Omega^2}{2N} \sum_{kk'} \left(\frac{1}{\Delta - \bar{\omega}_k} + \frac{1}{\Delta - \bar{\omega}_{k'}} \right) |k\rangle_e \langle k'|,$$

where the unperturbed Hamiltonian

$$H_0 = (2\Delta + U) |d\rangle \langle d| + \sum_k (\Delta + \bar{\omega}_k) |k\rangle_e \langle k| + \frac{\sqrt{2}\Omega}{\sqrt{N}} \sum_k (|k\rangle_e \langle d| + \text{H.c.})$$

and $\bar{\omega}_k = -i\Gamma - 2iJ_{\text{eff}} \cos k$.

The adiabatic elimination of two-excitation states $|kk'\rangle$ leads to the constant energy shift

$$\delta\omega = \frac{\Omega^2}{N} \sum_p \frac{1}{\Delta - \bar{\omega}_p} \sim -i \frac{\Omega^2 e^{i(\pi/4) \text{sgn}(\Delta)}}{\sqrt{2} |\Delta| \Gamma}$$

and the effective potential in the momentum space. The bound state

$$|\Psi_B\rangle = u |d\rangle + \sum_k f_k |k\rangle_e$$

of the effective Hamiltonian $H_{\text{eff}}^{(2)}$ satisfies

$$E_b u = (2\Delta + U)u + \frac{\sqrt{2}\Omega}{\sqrt{N}} \sum_k f_k, \\ E_b f_k = (\Delta + \bar{\varepsilon}_k) f_k + \frac{\sqrt{2}\Omega}{\sqrt{N}} u + \frac{\Omega^2}{2N} \sum_p \left(\frac{1}{\Delta - \bar{\omega}_k} + \frac{1}{\Delta - \bar{\omega}_p} \right) f_p, \quad (\text{C7})$$

where the bound state energy E_b corresponds to the poles of $D_f(\omega)$ and $\bar{\varepsilon}_k = \bar{\omega}_k + \delta\omega$.

The leading term of poles is determined by the Hamiltonian H_0 . For the resonant case $U = -\Delta$, H_0 is exactly the Hamiltonian in the single-excitation sector with $\Delta = 0$ and $\Omega \rightarrow \sqrt{2}\Omega$. Thus, the poles of $D_f(\omega)$ scale as $\Gamma^{-1/3}$. The subleading correction can be obtained by the solution of Eq. (C7). The solution

$$u = \frac{\sqrt{2}\Omega}{\varepsilon_b \sqrt{N}} \sum_k f_k$$

of u leads to the equation

$$\bar{\varepsilon}_k f_k + \frac{\Omega^2}{2N} \sum_p \left(\frac{1}{\Delta - \bar{\omega}_k} + \frac{1}{\Delta - \bar{\omega}_p} \right) f_p + \frac{2\Omega^2}{\varepsilon_b N} \sum_p f_p = \varepsilon_b f_k,$$

where $\varepsilon_b = E_b - \Delta$.

The formal solution

$$f_k = \Omega^2 \left[\frac{\frac{2}{\varepsilon_b} C_0 + \frac{1}{2} C_1}{\varepsilon_b - \bar{\varepsilon}_k} + \frac{C_0}{2(\Delta - \bar{\omega}_k)(\varepsilon_b - \bar{\varepsilon}_k)} \right]$$

is determined by two constants

$$C_0 = \frac{1}{N} \sum_p f_p, C_1 = \frac{1}{N} \sum_p \frac{1}{\Delta - \bar{\omega}_p} f_p.$$

The constants obey the self-consistent equations

$$C_0 = \left[\frac{2}{\varepsilon_b} I_1(\varepsilon_b) + \frac{1}{2} I_2(\varepsilon_b) \right] C_0 + \frac{1}{2} I_1(\varepsilon_b) C_1, \\ C_1 = \left[\frac{2}{\varepsilon_b} I_2(\varepsilon_b) + \frac{1}{2} I_3(\varepsilon_b) \right] C_0 + \frac{1}{2} I_2(\varepsilon_b) C_1,$$

where the integrals

$$I_1(\varepsilon_b) = \Omega^2 \int \frac{dk}{2\pi} \frac{1}{\varepsilon_b - \bar{\varepsilon}_k} = \Sigma_f(\varepsilon_b - \delta\omega), \\ I_2(\varepsilon_b) = \Omega^2 \int \frac{dk}{2\pi} \frac{1}{(\Delta - \bar{\omega}_k)(\varepsilon_b - \bar{\varepsilon}_k)} = \frac{\Sigma_f(\Delta) - \Sigma_f(\varepsilon_b - \delta\omega)}{\varepsilon_b - \delta\omega - \Delta}, \\ I_3(\varepsilon_b) = \Omega^2 \int \frac{dk}{2\pi} \frac{1}{(\Delta - \bar{\omega}_k)^2 (\varepsilon_b - \bar{\varepsilon}_k)} = -\partial_\Delta I_2(\varepsilon_b)$$

are evaluated analytically. Eventually, the poles of D^R can be determined by

$$\det \begin{pmatrix} \frac{2}{\varepsilon_b} I_1(\varepsilon_b) + \frac{1}{2} I_2(\varepsilon_b) - 1 & \frac{1}{2} I_1(\varepsilon_b) \\ \frac{2}{\varepsilon_b} I_2(\varepsilon_b) + \frac{1}{2} I_3(\varepsilon_b) & \frac{1}{2} I_2(\varepsilon_b) - 1 \end{pmatrix} = 0.$$

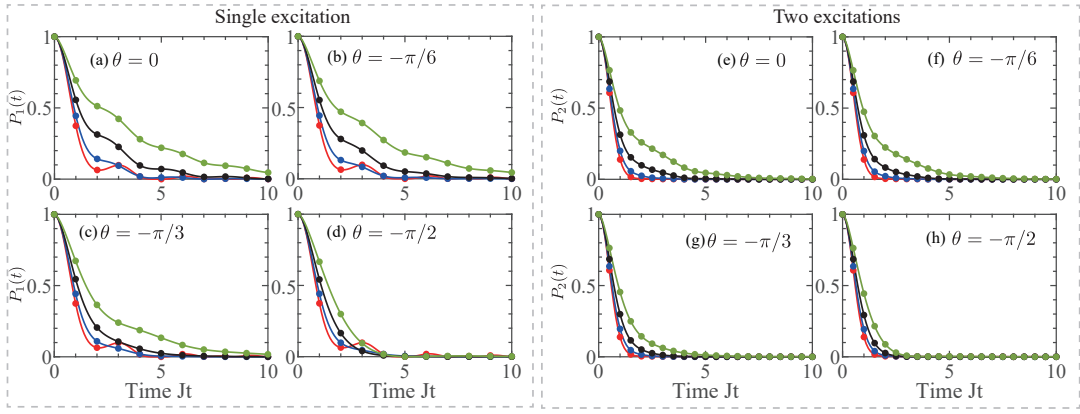


Figure 14. Spontaneous emission of (a) single excitation and (b) two excitations in an emitter coupled to a finite-size bath with various dissipation and coupling phase. In all panels, the solid line denotes the result obtained via the Green function approach with $\Omega/J = 1$, and $\Gamma/2J = 0.005, 0.3, 1.005, 3$ (red, blue, black, and green line, respectively); the dots denote the results obtained using the corresponding non-Hermitian Hamiltonian with the finite size $N_b = 60$. In (a), the single-excitation population $P_1(t)$ is obtained as a function of time t for $\Delta/J = 0$. In (b), the two-excitation population $P_2(t)$ is obtained for $\Delta/J = -U/J = -1$.

Appendix D: Scalings for arbitrary open baths

In this section, we present the detailed derivations leading to the results in Table I, for the open bath with arbitrary dissipative dispersions and dimensions.

We consider a tight-binding open bath with the dissipative band structure $\gamma(\mathbf{k})$ at dimensions $d = 1, 2, 3$. We concentrate on the purely dissipative bath and set $\epsilon(\mathbf{k}) = 0$. We denote the minimum dissipation rate as $\gamma_{\min} \equiv \min[\gamma(\mathbf{k})]$, which of course sits at the dissipation band edge, at some lattice momentum \mathbf{k}_0 . We assume the bath is spatially homogeneous. Near the band gap (edge) γ_{\min} , the dissipative dispersion can be approximated as

$$\gamma(\mathbf{k}) \approx \gamma_{\min} + c\Gamma|\mathbf{k} - \mathbf{k}_0|^\mu, \quad (\text{D1})$$

where the power μ depends on the specific form of $\gamma(\mathbf{k})$, the coefficient $c \propto a^\mu$ with a the lattice constant, and Γ is some dissipation energy scale. We define the number of the bath modes with the decay rate γ (i.e., dDOS) as $D_s(\gamma) := \int [d^d k / (2\pi)^d] \delta[\gamma - \gamma(\mathbf{k})]$. Near γ_{\min} , it follows from Eq. (D1) that

$$D_s(\gamma) = \frac{A}{(2\pi)^d} \frac{(\gamma - \gamma_{\min})^{-1+(d/\mu)}}{\mu(c\Gamma)^{d/\mu}}, \quad (\text{D2})$$

with $A = 2, 2\pi, 4\pi$ for dimension $d = 1, 2, 3$, respectively. Therefore, when $d/\mu < 1$, $\lim_{\gamma \rightarrow \gamma_{\min}} D_s(\gamma) \rightarrow \infty$, whereas for $d/\mu > 1$, $\lim_{\gamma \rightarrow \gamma_{\min}} D_s(\gamma) = 0$.

Now suppose an emitter with the on-site energy Δ is coupled to the open bath with a coupling rate Ω . We begin with $\Delta = 0$. Since the bath is purely dissipative, for convenience, we introduce $s = -i\omega$, so the poles of the single-particle Green function, corresponding to the quasibound states, are determined by

$$s + \Sigma(s) = 0, \quad (\text{D3})$$

where the self-energy function $\Sigma(s)$ associated with the purely dissipative open bath is given by

$$\Sigma(s) = \Omega^2 \int \frac{d^d k}{(2\pi)^d} \frac{1}{s + \gamma(\mathbf{k})}. \quad (\text{D4})$$

In the following, we analytically calculate Eq. (D4). Since the main contribution to the long-time emitter dynamics comes from the vicinity of γ_{\min} , we expand $\gamma(\mathbf{k})$ near γ_{\min} via Eq. (D1) and change the integral variable from the quasimomentum to γ via Eq. (D2). We obtain

$$\Sigma = \frac{A\Omega^2}{(2\pi)^d} \frac{1}{\mu(c\Gamma)^{d/\mu}} \int_{\gamma_{\min}}^{\Lambda} \frac{1}{s + \gamma} \frac{1}{(\gamma - \gamma_{\min})^{1-(d/\mu)}} d\gamma, \quad (\text{D5})$$

where we introduce a cutoff Λ . It follows from Eq. (D1) that $\Lambda \propto \Gamma$. Denoting $s' = s + \gamma_{\min}$ and $\Lambda' = \Lambda - \gamma_{\min}$, Eq. (D5) is calculated as

$$\begin{aligned} \Sigma &= \frac{A\Omega^2}{(2\pi)^d} \frac{(\Lambda')^{d/\mu}}{\mu(c\Gamma)^{d/\mu}} \frac{1}{s'} \int_0^1 \left(1 + \frac{\Lambda'}{s'} t\right)^{-1} t^{-1+(d/\mu)} dt \\ &= C \left(\frac{\Lambda'}{\Gamma}\right)^{d/\mu} \frac{1}{s'} F\left(1, \frac{d}{\mu}, \frac{d}{\mu} + 1; -\frac{\Lambda'}{s'}\right). \end{aligned} \quad (\text{D6})$$

Here, $F(\alpha, \beta, \zeta; z)$ is the hypergeometric function, and the precoefficient $C = B(\frac{d}{\mu}, 1) A \Omega^2 / [(2\pi)^d \mu c^{d/\mu}]$ with B the beta function.

By substituting Eq. (D6) into Eq. (D14), we can solve for the quasibound state solutions. We are interested in the regime $|\Lambda'/s'| \gg 1$ of Eq. (D6), corresponding to when Γ is the largest energy scale compared to all the other relevant scales as discussed in our manuscript. As such, we can expand the hypergeometric function in terms of the small parameter $|s'/\Lambda'| \ll 1$ and derive the analytical solutions at the leading order. In the following, we analyze the cases where $\gamma_{\min} \neq 0$ and $\gamma_{\min} = 0$, respectively.

- The bath has a dissipative gap ($\gamma_{\min} \neq 0$)

(i) When $d/\mu < 1$, we substitute $F[1, (d/\mu), (d/\mu) + 1; -(\Lambda'/s')] = [1 + (\Lambda'/s')]^{-d/\mu} F[(d/\mu), (d/\mu), (d/\mu) + 1; 1/(1 + \frac{s'}{\Lambda'})]$ in Eq. (D6). At the leading order of $|s'/\Lambda'| \ll 1$, we obtain $\Sigma(s) = C'(s + \gamma_{\min})^{-1+(d/\mu)} \Gamma^{-d/\mu}$, where $C' = CF[(d/\mu), (d/\mu), (d/\mu) + 1; 1]$ and we use $s = s' - \gamma_{\min}$. Inserting it into Eq. (D14), we find two quasibound states residing in the dissipative gap

$$s_1 = -C' \gamma_{\min}^{-1+(d/\mu)} \Gamma^{-d/\mu}, \quad (\text{D7})$$

$$s_2 = -\gamma_{\min} + \alpha \Gamma^{-1/(\mu/d-1)}, \quad (\text{D8})$$

with some coefficient α . The long-term emitter dynamics is determined by s_1 in Eq. (D7).

(ii) When $d/\mu > 1$, we insert $F[1, (d/\mu), (d/\mu) + 1; -(\Lambda'/s')] = [1 + (\Lambda'/s')]^{-1} F[1, 1, (d/\mu) + 1; 1/(1 + \frac{s'}{\Lambda'})] \approx (s'/\Lambda') F[1, 1, (d/\mu) + 1; 1]$ into Eq. (D6). Thus, at the leading order of $|s'/\Lambda'| \ll 1$, we obtain $\Sigma(s) = C''(\Lambda'^{-1+\frac{d}{\mu}}/\Gamma^{\frac{d}{\mu}}) = \tilde{C}'' \Gamma^{-1}$, with $C'' = CF[1, 1, (d/\mu) + 1; 1]$. Here, we exploit the fact that $\Lambda' = \Lambda - \gamma_{\min} \propto \Gamma$ according to Eq. (D2), with some constant \tilde{C}'' . In this case, we find one solution to Eq. (D14), describing a quasibound state in the dissipative gap:

$$s = -\tilde{C}'' \Gamma^{-1}. \quad (\text{D9})$$

(iii) When $d/\mu = 1$, we substitute $F[1, 1, 2; -(\Lambda'/s')] = [\ln(1 + \Lambda'/s')]/(\Lambda'/s')$ into Eq. (D6). At the leading order of $|s'/\Lambda'|$, we have $\Sigma(s) = C(\Lambda'^{\frac{d}{\mu}-1}/\Gamma^{\frac{d}{\mu}}) \ln(\Lambda'/s')$. Since $\Lambda' \propto \Gamma$ as mentioned before, for $|s| \ll \gamma_{\min} \ll \Gamma$, we have $\Sigma \approx \tilde{C}(1/\Gamma) \ln(\Lambda/\gamma_{\min})$. Inserting it into Eq. (D14), we find one quasibound state in the dissipative gap:

$$s = -\tilde{C} \frac{\ln(\frac{\Gamma}{\gamma_{\min}})}{\Gamma}. \quad (\text{D10})$$

- The bath has gapless dissipation ($\gamma_{\min} = 0$)

(i) When $d/\mu < 1$, at the leading order of $|s/\Lambda|$, we obtain $\Sigma(s) = C' s^{-1+(d/\mu)} \Gamma^{-d/\mu}$, with $C' = CF[(d/\mu), (d/\mu), (d/\mu)+1; 1]$. Therefore, Equation (D14) has solutions

$$s = (-C')^{1/(2-d/\mu)} \Gamma^{-1/(2\mu/d-1)}. \quad (\text{D11})$$

(ii) When $d/\mu > 1$, we obtain the leading expression $\Sigma(s) = \tilde{C}'' \Gamma^{-1}$, with $C'' = CF(1, 1, (d/\mu) + 1; 1)$. In this case, we find

$$s = -\tilde{C}'' \Gamma^{-1}, \quad (\text{D12})$$

which is the same as the gapped case.

(iii) When $d/\mu = 1$, we have the leading expression $\Sigma(s) = C(\Lambda^{\frac{d}{\mu}-1}/\Gamma^{\frac{d}{\mu}}) \ln(\Lambda/s)$. Considering $\Lambda \propto \Gamma$, we find

$$s = -\tilde{C} \frac{\ln(\frac{\Gamma}{\eta})}{\Gamma} \quad (\text{D13})$$

with some energy scale η .

When $\Delta \neq 0$, the quasibound state solutions are determined by

$$s - i\Delta + \Sigma(s) = 0. \quad (\text{D14})$$

We can redefine $\tilde{s} = s - i\Delta$ and then follow similar steps as before.

In summary, the above derivations lead to the results in Table I in the text.

Appendix E: Generic open bath with a finite size

In this section, we show that the emitter dynamics obtained from the Green function approach in Appendix A, though developed in the thermodynamic limit, remains valid for a finite-size bath under the condition

$$\alpha \equiv \frac{\Omega}{\delta\gamma} = \frac{\Omega}{2\pi^2} \frac{N_b^2}{\Gamma} \gg 1. \quad (\text{E1})$$

Here, Ω is the Rabi frequency, N_b is the finite size of the bath, $\delta\gamma$ is the dissipative gap, and Γ is the bath dissipation rate. Moreover, apart from the strong dissipation regime, we illustrate the emitter dynamics for a generic bath dissipation from the coherent limit $\Gamma/2J \rightarrow 0$ to the intermediate regime $\Gamma/2J \sim 1$ and for various coupling phases $\theta \in [0, -\pi/2]$.

We first validate the Green function approach for a finite-size, strongly dissipative, bath in three scenarios: $\alpha < 1$, $\alpha \sim 1$, and $\alpha > 1$, respectively. For the spontaneous emission of a single excitation in an emitter, we compare the results obtained from two approaches: (i) We compute the population dynamics of single excitation, $P_1(t)$, by numerically evolving the state via the non-Hermitian emitter-bath Hamiltonian in Eq. (9) with $U = 0$; (ii) we use $P_1(t) = |G(t)|^2$ with $G(t)$ in Eq. (A4). We remark that Eq. (E1) indicates α depends on both Γ and N_b . In Fig. 13(a), we change N_b and fix Γ . The black curve denotes the emitter dynamics from the Green function function, i.e., as in the thermodynamic limit, while the dashed curves denote the results from the approach (i) for various N_b . We see that when $\alpha < 1$, the finite-size dynamics is significantly different from that in the thermodynamic limit, but the two becomes compatible with each other when N_b is increased to $\alpha \gg 1$. In Fig. 13(b), we change Γ and fix N_b . As shown, the two approaches agree well with each other by choosing a smaller Γ so that $\alpha \gg 1$.

Although our key results in the main text are for the strongly open bath, our developed approach applies to arbitrary parameter regimes of the bath. In Fig. 14(a), we present the dynamics of single excitation with the detuning $\Delta = 0$, when a bath of the size $N_b = 60$ is nearly coherent $\Gamma/2J \rightarrow 0$, weakly dissipative $\Gamma/2J < 1$, and in the intermediate regimes $\Gamma/2J \gtrsim 1$. We consider $\theta = 0, -\pi/6, -\pi/3, -\pi/2$, respectively. As $\alpha \gg 1$, we see

that the results from the Green function approach (solid curves) agree well with the time evolution via the non-Hermitian (dots). In Fig. 14(b), we show the spontaneous emissions of two excitations in an emitter coupled to the bath with the finite size $N_b = 60$ and various Γ . The solid

curves denote the results obtained from $P_2(t) = |D(t)|^2$, where $D(t)$ is the Fourier transform of the fictitious two-particle Green function (A9). The dotted lines denote the calculation of $P_2(t)$ via the non-Hermitian Hamiltonian in Eq. (27) of the main text. Again, we find perfect good agreement between the two.

* tshi@itp.ac.cn

† huying@sxu.edu.cn

- [1] C. M. Bender and S. Boettcher, Real Spectra in Non-Hermitian Hamiltonians Having PT Symmetry, *Phys. Rev. Lett.* **80**, 5243 (1998).
- [2] S. Yao and Z. Wang, Edge States and Topological Invariants of Non-Hermitian Systems, *Phys. Rev. Lett.* **121**, 086803 (2018).
- [3] F. K. Kunst, E. Edvardsson, J. C. Budich, and E. J. Bergholtz, Biorthogonal Bulk-Boundary Correspondence in Non-Hermitian Systems, *Phys. Rev. Lett.* **121**, 026808 (2018).
- [4] Z. Gong, Y. Ashida, K. Kawabata, K. Takasan, S. Higashikawa, and M. Ueda, Topological Phases of Non-Hermitian Systems, *Phys. Rev. X* **8**, 031079 (2018).
- [5] H. Zhou, C. Peng, Y. Yoon, C. W. Hsu, K. A. Nelson, L. Fu, J. D. Joannopoulos, M. Soljačić, and B. Zhen, Observation of Bulk Fermi Arc and Polarization Half Charge from Paired Exceptional Points, *Science* **359**, 1009 (2018).
- [6] K. Kawabata, K. Shiozaki, M. Ueda, and M. Sato, Symmetry and Topology in Non-Hermitian Physics, *Phys. Rev. X* **9**, 041015 (2019).
- [7] L. Xiao, T. Deng, K. Wang, G. Zhu, Z. Wang, W. Yi, and P. Xue, Non-Hermitian Bulk-Boundary Correspondence in Quantum Dynamics, *Nat. Phys.* **16**, 761 (2020).
- [8] C. C. Wanjura, M. Brunelli, and A. Nunnenkamp, Topological Framework for Directional Amplification in Driven-Dissipative Cavity Arrays, *Nat. Commun.* **11**, 3149 (2020).
- [9] K. Wang, A. Dutt, C. C. Wojcik, and S. Fan, Topological Complex-Energy Braiding of Non-Hermitian Bands, *Nature (London)* **598**, 59 (2021).
- [10] E. J. Bergholtz, J. C. Budich, and F. K. Kunst, Exceptional Topology of Non-Hermitian Systems, *Rev. Mod. Phys.* **93**, 015005 (2021).
- [11] K. Fang, J. Luo, A. Metelmann, M. H. Matheny, F. Marquardt, A. A. Clerk, and O. Painter, Generalized Non-reciprocity in an Optomechanical Circuit via Synthetic Magnetism and Reservoir Engineering, *Nat. Phys.* **13**, 465 (2017).
- [12] L. Xiao, X. Zhan, Z. H. Bian, K. K. Wang, X. Zhang, X. P. Wang, J. Li, K. Mochizuki, D. Kim, N. Kawakami, W. Yi, H. Obuse, B. C. Sanders, and P. Xue, Observation of Topological Edge States in Parity-Time-Symmetric Quantum Walks, *Nat. Phys.* **13**, 1117 (2017).
- [13] F. E. Öztürk, T. Lappe, G. Hellmann, J. Schmitt, J. Klaers, F. Vewinger, J. Kroha, and M. Weitz, Observation of a Non-Hermitian Phase Transition in an Optical Quantum Gas, *Science* **372**, 88 (2021).
- [14] P. Peng, W. Cao, C. Shen, W. Qu, J. Wen, L. Jiang, and Y. Xiao, Anti-Parity-Time Symmetry with Flying Atoms, *Nat. Phys.* **12**, 1139 (2016).
- [15] J. Li, A. K. Harter, J. Liu, L. d. Melo, Y. N. Joglekar, and L. Luo, Observation of Parity-Time Symmetry Breaking Transitions in a Dissipative Floquet System of Ultracold Atoms, *Nat. Commun.* **10**, 855 (2019).
- [16] Y. Takasu, T. Yagami, Y. Ashida, R. Hamazaki, Y. Kuno, and Y. Takahashi, PT-Symmetric Non-Hermitian Quantum Many-Body System Using Ultracold Atoms in an Optical Lattice with Controlled Dissipation, *Prog. Theor. Exp. Phys.* **2020**, pta094 (2020).
- [17] D. Hao, L. Wang, X. Lu, X. Cao, S. Jia, Y. Hu, and Y. Xiao, Topological Atomic Spin Wave Lattices by Dissipative Couplings, *Phys. Rev. Lett.* **130**, 153602 (2023).
- [18] Q. Liang, D. Xie, Z. Dong, H. Li, H. Li, B. Gadway, W. Yi, and B. Yan, Dynamic Signatures of Non-Hermitian Skin Effect and Topology in Ultracold Atoms, *Phys. Rev. Lett.* **129**, 070401 (2022).
- [19] Y. Wu, W. Liu, J. Geng, X. Song, X. Ye, C.-K. Duan, X. Rong, and J. Du, Observation of Parity-Time Symmetry Breaking in a Single-Spin System, *Science* **364**, 878 (2019).
- [20] M. Naghiloo, M. Abbasi, Y. N. Joglekar, and K. W. Murch, Quantum State Tomography across the Exceptional Point in a Single Dissipative Qubit, *Nat. Phys.* **15**, 1232 (2019).
- [21] C. Leefmans, A. Dutt, J. Williams, L. Yuan, M. Parto, F. Nori, S. Fan, and A. Marandi, Topological Dissipation in a Time-Multiplexed Photonic Resonator Network, *Nat. Phys.* **18**, 442 (2022).
- [22] L. Pickup, H. Sigurdsson, J. Ruostekoski, and P. G. Lagoudakis, Synthetic Band-Structure Engineering in Polariton Crystals with Non-Hermitian Topological Phases, *Nat. Commun.* **11**, 4431 (2020).
- [23] N. Pernet, P. St-Jean, D. D. Solnyshkov, G. Malpuech, N. C. Zambon, Q. Fontaine, B. Real, O. Jamadi, A. Lemaitre, M. Morassi, L. L. Gratiet, T. Baptiste, A. Harouri, I. Sagnes, A. Amo, S. Ravets, and J. Bloch, Gap Solitons in a One-Dimensional Driven-Dissipative Topological Lattice, *Nat. Phys.* **18**, 678 (2022).
- [24] S. Longhi, Quantum Decay and Amplification in a Non-Hermitian Unstable Continuum, *Phys. Rev. A* **93**, 062129 (2016).
- [25] M. Nakagawa, N. Kawakami, and M. Ueda, Non-Hermitian Kondo Effect in Ultracold Alkaline-Earth Atoms, *Phys. Rev. Lett.* **121**, 203001 (2018).
- [26] K. Yamamoto, M. Nakagawa, K. Adachi, K. Takasan, M. Ueda, and N. Kawakami, Theory of Non-Hermitian Fermionic Superfluidity with a Complex-Valued Interaction, *Phys. Rev. Lett.* **123**, 123601 (2019).
- [27] S. Gopalakrishnan and M. J. Gullans, Entanglement and Purification Transitions in Non-Hermitian Quantum Mechanics, *Phys. Rev. Lett.* **126**, 170503 (2021).
- [28] F. Roccati, S. Lorenzo, G. Calajò, G. M. Palma, A. Carollo, and F. Ciccarello, Exotic Interactions Mediated by

- a Non-Hermitian Photonic Bath, *Optica* **9**, 565 (2022).
- [29] Z. Gong, M. Bello, D. Malz, and F. K. Kunst, Bound States and Photon Emission in Non-Hermitian Nanophotonics, *Phys. Rev. A* **106**, 053517 (2022).
- [30] Z. Gong, M. Bello, D. Malz, and F. K. Kunst, Anomalous Behaviors of Quantum Emitters in Non-Hermitian Baths, *Phys. Rev. Lett.* **129**, 223601 (2022).
- [31] J. F. Poyatos, J. I. Cirac, and P. Zoller, Quantum Reservoir Engineering with Laser Cooled Trapped Ions, *Phys. Rev. Lett.* **77**, 4728 (1996).
- [32] S. Diehl, A. Micheli, A. Kantian, B. Kraus, H. P. Büchler, and P. Zoller, Quantum States and Phases in Driven Open Quantum Systems with Cold Atoms, *Nat. Phys.* **4**, 878 (2008).
- [33] F. Verstraete, M. M. Wolf, and J. I. Cirac, Quantum Computation and Quantum-State Engineering Driven by Dissipation, *Nat. Phys.* **5**, 633 (2009).
- [34] S. Diehl, E. Rico, M. A. Baranov, and P. Zoller, Topology by Dissipation in Atomic Quantum Wires, *Nat. Phys.* **7**, 971 (2011).
- [35] M. Müller, S. Diehl, G. Pupillo, and P. Zoller, Engineered Open Systems and Quantum Simulations with Atoms and Ions, *Adv. At. Mol. Opt. Phys.* **61**, 1 (2012).
- [36] A. Tomadin, S. Diehl, M. D. Lukin, P. Rabl, and P. Zoller, Reservoir Engineering and Dynamical Phase Transitions in Optomechanical Arrays, *Phys. Rev. A* **86**, 033821 (2012).
- [37] J. S. Douglas, H. Habibian, C.-L. Hung, A. V. Gorshkov, H. J. Kimble, and D. E. Chang, Quantum Many-Body Models with Cold Atoms Coupled to Photonic Crystals, *Nat. Photonics* **9**, 326 (2015).
- [38] T. Ramos, H. Pichler, A. J. Daley, and P. Zoller, Quantum Spin Dimers from Chiral Dissipation in Cold-Atom Chains, *Phys. Rev. Lett.* **113**, 237203 (2014).
- [39] D. E. Chang, J. S. Douglas, A. González-Tudela, C.-L. Hung, and H. J. Kimble, Colloquium: Quantum Matter Built from Nanoscopic Lattices of Atoms and Photons, *Rev. Mod. Phys.* **90**, 031002 (2018).
- [40] Z.-P. Cian, G. Zhu, S.-K. Chu, A. Seif, W. DeGottardi, L. Jiang, and Mohammad Hafezi, Photon Pair Condensation by Engineered Dissipation, *Phys. Rev. Lett.* **123**, 063602 (2019).
- [41] P. M. Harrington, E. J. Mueller, and K. W. Murch, Engineered Dissipation for Quantum Information Science, *Nat. Rev. Phys.* **4**, 660 (2022).
- [42] H. Paul, Photon Antibunching, *Rev. Mod. Phys.* **54**, 1061 (1982).
- [43] M. Bamba, A. Imamoğlu, I. Carusotto, and C. Ciuti, Origin of Strong Photon Antibunching in Weakly Nonlinear Photonic Molecules, *Phys. Rev. A* **83**, 021802(R) (2011).
- [44] X. Kong, C. Navarrete-Benlloch, and Y. Chang, Accessing Strongly-Coupled Systems without Compromising Them, arXiv:2204.04212.
- [45] A. V. Balatsky, I. Vekhter, and J.-X. Zhu, Impurity-Induced States in Conventional and Unconventional Superconductors, *Rev. Mod. Phys.* **78**, 373 (2006).
- [46] K. L. Hur, Kondo Resonance of a Microwave Photon, *Phys. Rev. B* **85**, 140506(R) (2012).
- [47] M. Goldstein, M. H. Devoret, M. Houzet, and L. I. Glazman, Inelastic Microwave Photon Scattering off a Quantum Impurity in a Josephson-Junction Array, *Phys. Rev. Lett.* **110**, 017002 (2013).
- [48] T. Shi, Y.-H. Wu, A. González-Tudela, and J. I. Cirac, Bound States in Boson Impurity Models, *Phys. Rev. X* **6**, 021027 (2016).
- [49] S. John and J. Wang, Quantum Electrodynamics near a Photonic Band Gap: Photon Bound States and Dressed Atoms, *Phys. Rev. Lett.* **64**, 2418 (1990).
- [50] H. Nakazato, M. Namiki, and S. Pascazio, Temporal Behavior of Quantum Mechanical Systems, *Int. J. Mod. Phys. B* **10**, 247 (1996).
- [51] R. O. Umucalılar and I. Carusotto, Fractional Quantum Hall States of Photons in an Array of Dissipative Coupled Cavities, *Phys. Rev. Lett.* **108**, 206809 (2012).
- [52] A. González-Tudela, V. Paulisch, D. E. Chang, H. J. Kimble, and J. I. Cirac, Deterministic Generation of Arbitrary Photonic States Assisted by Dissipation, *Phys. Rev. Lett.* **115**, 163603 (2015).
- [53] I. Söllner, S. Mahmoodian, S. L. Hansen, L. Midolo, A. Javadi, G. Kiršanskė, T. Pregolato, H. El-Ella, E. H. Lee, J. D. Song, S. Stobbe, and P. Lodahl, Deterministic Photon-Emitter Coupling in Chiral Photonic Circuits, *Nat. Nanotechnol.* **10**, 775 (2015).
- [54] T. Ramos, B. Vermersch, P. Hauke, H. Pichler, and P. Zoller, Non-Markovian Dynamics in Chiral Quantum Networks with Spins and Photons, *Phys. Rev. A* **93**, 062104 (2016).
- [55] Y. Liu and A. A. Houck, Quantum Electrodynamics near a Photonic Bandgap, *Nat. Phys.* **13**, 48 (2017).
- [56] T. Shi, H. J. Kimble, and J. I. Cirac, Topological Phenomena in Classical Optical Networks, *Proc. Natl. Acad. Sci. U.S.A.* **114**, E8967 (2017).
- [57] A. González-Tudela and J. I. Cirac, Exotic Quantum Dynamics and Purely Long-Range Coherent Interactions in Dirac Conelike Baths, *Phys. Rev. A* **97**, 043831 (2018).
- [58] T. Shi, Y.-H. Wu, A. González-Tudela, and J. I. Cirac, Effective Many-Body Hamiltonians of Qubit-Photon Bound States, *New J. Phys.* **20**, 105005 (2018).
- [59] M. Bello, G. Platero, J. I. Cirac, and A. González-Tudela, Unconventional Quantum Optics in Topological Waveguide QED, *Sci. Adv.* **5**, eaaw0297 (2019).
- [60] J. Argüello-Luengo, A. González-Tudela, T. Shi, P. Zoller, and J. I. Cirac, Analogue Quantum Chemistry Simulation, *Nature (London)* **574**, 215 (2019).
- [61] J. Argüello-Luengo, A. González-Tudela, T. Shi, P. Zoller, and J. I. Cirac, Quantum Simulation of Two-Dimensional Quantum Chemistry in Optical Lattices, *Phys. Rev. Res.* **2**, 042013(R) (2020).
- [62] J. Argüello-Luengo, T. Shi, and A. González-Tudela, Engineering Analog Quantum Chemistry Hamiltonians Using Cold Atoms in Optical Lattices, *Phys. Rev. A* **103**, 043318 (2021).
- [63] T. Shi, D. E. Chang, and J. I. Cirac, Multiphoton-Scattering Theory and Generalized Master Equations, *Phys. Rev. A* **92**, 053834 (2015).
- [64] Y. Chang, A. González-Tudela, C. S. Muñoz, C. Navarrete-Benlloch, and T. Shi, Deterministic Down-Converter and Continuous Photon-Pair Source within the Bad-Cavity Limit, *Phys. Rev. Lett.* **117**, 203602 (2016).
- [65] J. Dalibard, Y. Castin, and K. Mølmer, Wave-Function Approach to Dissipative Processes in Quantum Optics, *Phys. Rev. Lett.* **68**, 580 (1992).
- [66] A. J. Daley, Quantum Trajectories and Open Many-Body Quantum Systems, *Adv. Phys.* **63**, 77 (2014).
- [67] J. Rammer, *Quantum Field Theory of Non-equilibrium States* (Cambridge University Press, Cambridge, England, 2007).
- [68] L. M. Sieberer, M. Buchhold, and S. Diehl, Keldysh Field

- Theory for Driven Open Quantum Systems, Rep. Prog. Phys. **79**, 096001 (2016).
- [69] B. Misra and E. C. G. Sudarshan, The Zeno's Paradox in Quantum Theory, J. Math. Phys. (N.Y.) **18**, 756 (1977).
- [70] W. M. Itano, D. J. Heinzen, J. J. Bollinger, and D. J. Wineland, Quantum Zeno Effect, Phys. Rev. A **41**, 2295 (1990).
- [71] M. O. Scully and M. S. Zubairy, Quantum Optics (Cambridge University Press, Cambridge, England, 1997).
- [72] Xiang-Bin Wang, J. Q. You, and F. Nori, Quantum Entanglement via Two-Qubit Quantum Zeno Dynamics, Phys. Rev. A **77**, 062339 (2008).
- [73] S. Maniscalco, F. Francica, R. L. Zaffino, N. L. Gullo, and F. Plastina, Protecting Entanglement via the Quantum Zeno Effect, Phys. Rev. Lett. **100**, 090503 (2008).
- [74] N. Syassen, D. M. Bauer, M. Lettner, T. Volz, D. Dietze, J. J. García-Ripoll, J. I. Cirac, G. Rempe, and S. Dürr, Strong Dissipation Inhibits Losses and Induces Correlations in Cold Molecular Gases, Science **320**, 1329 (2008).
- [75] Y.-J. Han, Y.-H. Chan, W. Yi, A. J. Daley, S. Diehl, P. Zoller, and L.-M. Duan, Stabilization of the p-Wave Superfluid State in an Optical Lattice, Phys. Rev. Lett. **103**, 070404 (2009).
- [76] A. Signoles, A. Facon, D. Grosso, I. Dotsenko, S. Haroche, Jean-Michel Raimond, M. Brune, and S. Gleyzes, Confined Quantum Zeno Dynamics of a Watched Atomic Arrow, Nat. Phys. **10**, 715 (2014).
- [77] Y. Hu, Z. Cai, M. A. Baranov, and P. Zoller, Majorana Fermions in Noisy Kitaev Wires, Phys. Rev. B **92**, 165118 (2015).
- [78] H. Fröml, C. Muckel, C. Kollath, A. Chiochetta, and S. Diehl, Ultracold Quantum Wires with Localized Losses: Many-Body Quantum Zeno Effect, Phys. Rev. B **101**, 144301 (2020).
- [79] E. M. Kessler, Generalized Schrieffer-Wolff Formalism for Dissipative Systems, Phys. Rev. A **86**, 012126 (2012).
- [80] F. Reiter and A. S. Sørensen, Effective Operator Formalism for Open Quantum Systems, Phys. Rev. A **85**, 032111 (2012).
- [81] See details in the Appendixes **A** and **C**.
- [82] T. Shi, S. Fan, and C. P. Sun, Two-Photon Transport in a Waveguide Coupled to a Cavity in a Two-Level System, Phys. Rev. A **84**, 063803 (2011).
- [83] T. Shi and S. Fan, Two-Photon Transport through a Waveguide Coupling to a Whispering-Gallery Resonator Containing an Atom and Photon-Blockade Effect, Phys. Rev. A **87**, 063818 (2013).
- [84] Y.-X. Zhang and K. Mølmer, Theory of Subradiant States of a One-Dimensional Two-Level Atom Chain, Phys. Rev. Lett. **122**, 203605 (2019).
- [85] This approximation is generally good if the major contribution to $\int (d\omega/2\pi) G_f(\omega) e^{-i\omega t}$ comes from the residue associated with $\epsilon_s^{(1)}$.
- [86] N. Goldman, J. C. Budich, and P. Zoller, Topological Quantum Matter with Ultracold Gases in Optical Lattices, Nat. Phys. **12**, 639 (2016).